

Saddle Invariant Objects and their Global Manifolds in a Neighborhood of a Homoclinic Flip Bifurcation of Case B

Andrus Giraldo[†], Bernd Krauskopf[†], and Hinke M. Osinga[†]

July 29, 2022

Abstract

When a real saddle equilibrium in a three-dimensional vector field undergoes a homoclinic bifurcation, the associated two-dimensional invariant manifold of the equilibrium closes on itself in an orientable or non-orientable way, provided the corresponding genericity conditions. We are interested in the interaction between global invariant manifolds of saddle equilibria and saddle periodic orbits for a vector field close to a codimension-two homoclinic flip bifurcation, that is, the point of transition between having an orientable or non-orientable two-dimensional surface. Here, we focus on homoclinic flip bifurcations of case **B**, which is characterized by the fact that the codimension-two point gives rise to an additional homoclinic bifurcation, namely, a two-homoclinic orbit. To explain how the global manifolds organize phase space, we consider Sandstede's three-dimensional vector field model, which features inclination and orbit flip bifurcations. We compute global invariant manifolds and their intersection sets with a suitable sphere, by means of continuation of suitable two-point boundary problems, to understand their role as separatrices of basins of attracting periodic orbits. We show representative images in phase space and on the sphere, such that we can identify topological properties of the manifolds in the different regions of parameter space and at the homoclinic bifurcations involved. We find heteroclinic orbits between saddle periodic orbits and equilibria, which give rise to regions of infinitely many heteroclinic orbits. Additional equilibria exist in Sandstede's model and we compactify phase space to capture how equilibria may emerge from or escape to infinity. We present images of these bifurcation diagrams, where we outline different configurations of equilibria close to homoclinic flip bifurcations of case **B**; furthermore, we characterize the dynamics of Sandstede's model at infinity.

1 Introduction

Dynamical systems has been an active area of research since the work of Henri Poincaré on celestial mechanics [35]. More recently, the bifurcation theory of dynamical systems has become a tool for understanding different phenomena, as far ranging as the excitation of neurons [10, 14, 19], turbulence in fluid flows [37, 43], and the dynamics of laser systems [36, 45]; more applications can be found, for example, in [13, 42]. The models arising in such applications are typically vector fields of the form

$$\dot{x} = f(x, \mu), \quad (1)$$

where $x \in \mathbb{R}^n$ is the state, $\mu \in \mathbb{R}^m$ is a (multi)parameter and $f : \mathbb{R}^n \times \mathbb{R}^m \rightarrow \mathbb{R}^n$ is a sufficiently smooth function. For any fixed value of μ , equation (1) defines a flow ϕ^t on the phase space \mathbb{R}^n for all $t \in \mathbb{R}$. In bifurcation theory, one wants to understand how the phase portrait of this flow ϕ^t changes topologically when μ is varied. One way for such topological changes to occur is through changes of stabilities of equilibria and periodic orbits in phase space. These are known in the literature as *local bifurcations*; and they have been studied in detail by normal forms and desingularization techniques [13, 22, 34, 42]. *Global bifurcations*, on the other hand, are topological changes arising from interactions between global invariant manifolds of saddle equilibria and saddle periodic orbits, which can re-arrange to change the phase space globally. In particular, the existence of homoclinic or heteroclinic orbits, which are connecting orbits between saddle

[†]Department of Mathematics, The University of Auckland, Private Bag 92019, Auckland 1142, New Zealand (a.giraldo@auckland.ac.nz, b.krauskopf@auckland.ac.nz, h.m.osinga@auckland.ac.nz)

equilibria and/or saddle periodic orbits, can have dramatic effects, for example, regarding the existence and size of basins of attractions.

We are interested in gaining a better understanding of a special type of global bifurcation that is known as *homoclinic flip bifurcation*; it can occur in vector fields of dimension three or higher. This bifurcation concerns a real saddle equilibrium and a homoclinic orbit, that is, a connecting orbit of the equilibrium back to itself, such that the associated invariant manifolds are neither orientable or non-orientable; see section 2.1 for details. To study this bifurcation, we work with the three-dimensional vector field

$$X^s(x, y, z) : \begin{cases} \dot{x} = P^1(x, y, z) := ax + by - ax^2 + (\tilde{\mu} - \alpha z)x(2 - 3x), \\ \dot{y} = P^2(x, y, z) := bx + ay - \frac{3}{2}bx^2 - \frac{3}{2}axy - 2y(\tilde{\mu} - \alpha z), \\ \dot{z} = P^3(x, y, z) := cz + \mu x + \gamma xz + \alpha\beta(x^2(1 - x) - y^2). \end{cases} \quad (2)$$

It was introduced by Sandstede in [39], who studied this model with additional z -dependent terms in the equations for x and y , which are controlled by a parameter δ in [39] that we set to 0 in (2). We choose the parameters such that the origin $\mathbf{0} \in \mathbb{R}^3$ is a saddle equilibrium of system (2) whose linearization has two different negative and one positive eigenvalues $\lambda^{ss} < \lambda^s < 0 < \lambda^u$; see section 2.2. The other case of a real saddle, that is, an equilibrium with two positive and one negative eigenvalues can be reduced to this case by reversing time. Since the origin is hyperbolic, the Stable Manifold Theorem [33] implies the existence of an immersed two-dimensional stable manifold $W^s(\mathbf{0})$ and an immersed one-dimensional unstable manifold $W^u(\mathbf{0})$; the stable manifold $W^s(\mathbf{0})$ is a surface foliated by orbits that converge to $\mathbf{0}$ as $t \rightarrow \infty$, and $W^u(\mathbf{0})$ consist of two orbits that converge to $\mathbf{0}$ as $t \rightarrow -\infty$.

We can choose α, μ and $\tilde{\mu}$ such that a homoclinic bifurcation occurs: this means that there exists an orbit Γ_{hom} that converges to $\mathbf{0}$ both as $t \rightarrow \infty$ and as $t \rightarrow -\infty$; that is, one of the branches of $W^u(\mathbf{0})$ lies entirely in $W^s(\mathbf{0})$. Consequently, under certain genericity conditions that are outlined in section 2.1, the respective local part of $W^s(\mathbf{0})$ closes back on itself and is either topologically equivalent to a cylinder or a Möbius band, which classifies the homoclinic bifurcation as orientable or non-orientable, respectively [4, 15, 20, 47]. fig. 1 shows two homoclinic orbits of system (2), together with the associated stable and unstable manifolds of $\mathbf{0}$; they share the same parameter values except that $\alpha = 0.3$ in column (a) and $\alpha = 0.65$ in column (b). The top row shows a linear approximation of $W^s(\mathbf{0})$ around the homoclinic orbit Γ_{hom} , which is computed as the span of the tangent vectors of $W^s(\mathbf{0})$ around Γ_{hom} . The bottom row shows $W^s(\mathbf{0})$ in a larger region of phase space. The stable manifold $W^s(\mathbf{0})$ is rendered in two shades of blue to illustrate the orientability properties of the manifold. In fig. 1 panel (a1) we see that $W^s(\mathbf{0})$, locally near Γ_{hom} , is a topological cylinder; while in panel (b1), this local part of $W^s(\mathbf{0})$ is a topological Möbius band. Indeed fig. 1 illustrates how $W^s(\mathbf{0})$ closes on itself along the strong stable manifold $W^{ss}(\mathbf{0})$ at the moment of an orientable homoclinic bifurcation in column (a); and the non-orientable case in column (b).

Generically, homoclinic orbits as shown in fig. 1 exist at codimension-one bifurcations [22, 40]. We are interested in the case when one of the genericity conditions is not valid, such that the homoclinic bifurcation has codimension-two. More precisely, we study the case where $W^s(\mathbf{0})$ transitions from being orientable to being non-orientable. This codimension-two point is called a *homoclinic flip bifurcation* and it may be an *inclination* or an *orbit flip bifurcation* [18]. There are three different codimension-two unfoldings of homoclinic flip bifurcation, called cases **A**, **B** and **C**, for both an inclination and an orbit flip bifurcation; these have been studied theoretically with methods including return maps [4, 15], Shilnikov variables [20] and Lin's method [38]. The theoretical results describe the unfoldings of the dynamics locally in a small tubular neighbourhood of the homoclinic orbit. A “more global” approach, which relies on numerical computations, has been used in [1] to understand how the global manifolds re-arrange phase space for the simplest case **A**. Already for this case an extra bifurcating branch of heteroclinic folds was found that had previously not been identified.

Compared with case **A**, cases **B** and **C** are richer with respect to the invariant objects that are created and destroyed close to the homoclinic flip bifurcation. In case **A** a single attracting (or repelling) periodic orbit is created. The unfolding of case **B**, on the other hand, involves saddle periodic orbits, a period doubling and an additional homoclinic bifurcation curve; see section 3 and fig. 5. Finally, in the unfolding of case **C** it has been proved that there exists a period-doubling cascade, region of horseshoe dynamics, n -homoclinic orbits (for any $n \in \mathbb{N}$) and strange attractors [4, 17, 18, 29, 30]. Additionally, case **C** has been identified as an organizing center for the creation of spikes of periodic orbits in the Hindmarsh-Rose model that describes the essential spiking behaviour of a neuron [23].

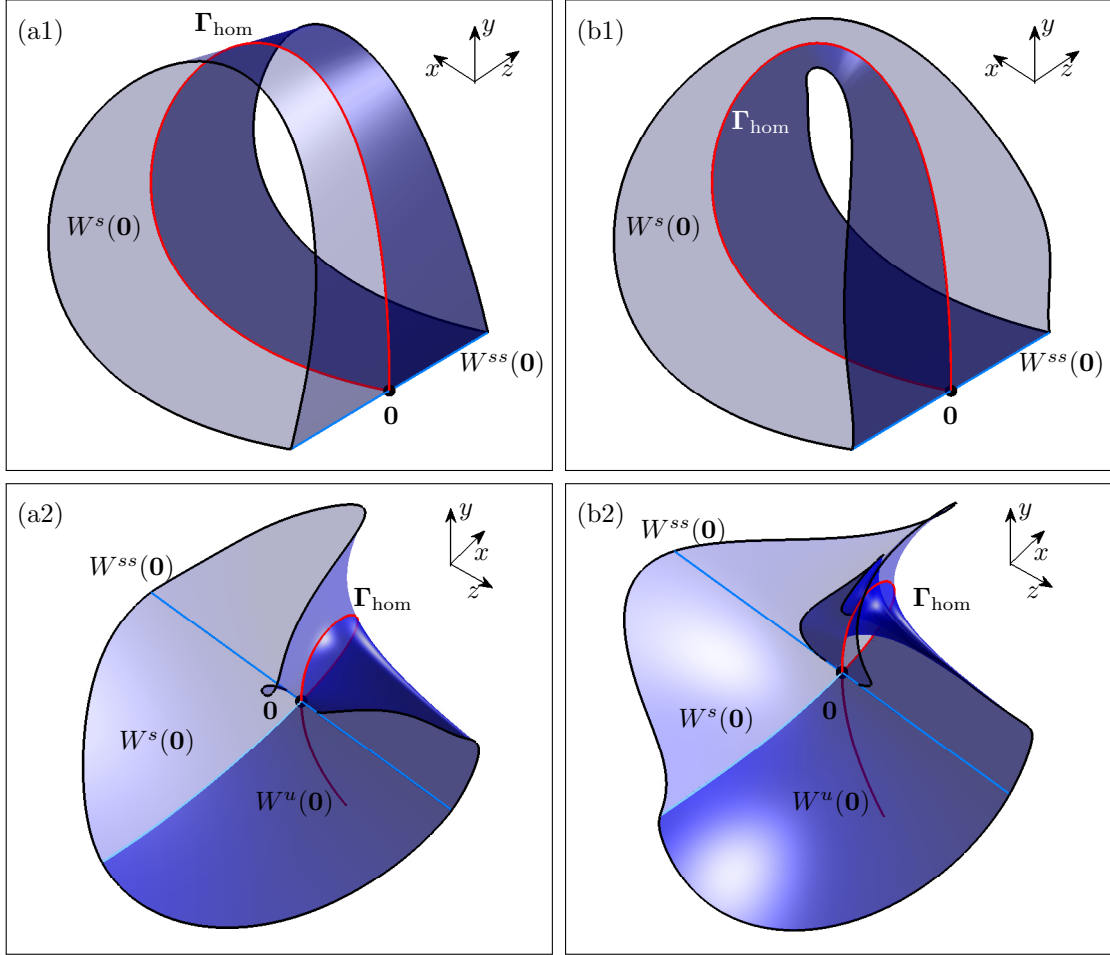


Figure 1: The stable manifold $W^s(\mathbf{0})$ of system (2) at a codimension-one homoclinic bifurcation in \mathbb{R}^3 . Column (a) shows an orientable and column (b) a non-orientable homoclinic orbit. The top row illustrates the tangent space of $W^s(\mathbf{0})$ around Γ_{hom} . The bottom row shows a portion of $W^s(\mathbf{0})$ in phase space. Shown are $W^s(\mathbf{0})$ as a rendered surface with one half colored dark-blue and the other half light-blue, the one-dimensional strong stable manifold $W^{ss}(\mathbf{0})$ as a light blue curve and the unstable manifold $W^u(\mathbf{0})$ as a red curve. Column (a) is for $(a, b, c, \alpha, \beta, \gamma, \mu, \tilde{\mu}) = (0.22, 1, -2, 0.3, 1, 2, 0, 0)$ and column (b) for $(a, b, c, \alpha, \beta, \gamma, \mu, \tilde{\mu}) = (0.22, 1, -2, 0.65, 1, 2, 0, 0)$.

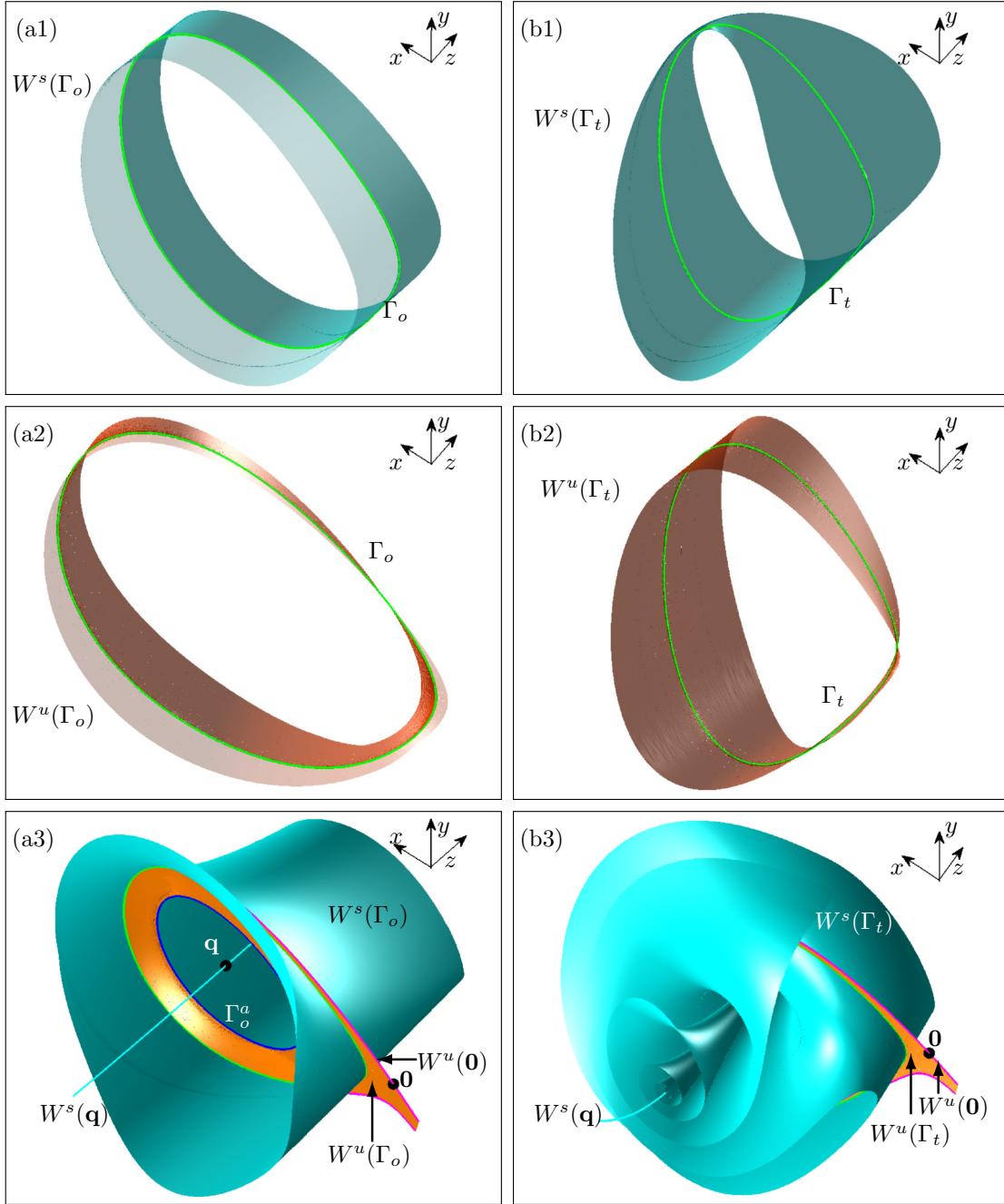


Figure 2: The stable manifolds $W^s(\Gamma_o)$ and $W^s(\Gamma_t)$, and unstable manifolds $W^u(\Gamma_o)$ and $W^u(\Gamma_t)$ of periodic orbits Γ_o and Γ_t in system (2). Column (a) shows the orientable and column (b) the non-orientable case. The top row shows $W^s(\Gamma_o)$ and $W^s(\Gamma_t)$ in a small tubular neighborhood of Γ_o and Γ_t , respectively, while the middle row shows the $W^u(\Gamma_o)$ and $W^u(\Gamma_t)$ in this same small tubular neighborhood. The bottom row, shows a large portion of these manifolds and how they are interacting with other one-dimensional manifolds in phase space. Shown are $W^s(\Gamma_o)$ and $W^s(\Gamma_t)$ as cyan surfaces, $W^u(\Gamma_o)$ and $W^u(\Gamma_t)$ as orange surfaces, Γ_o and Γ_t as green curves, Γ_o^a as a blue curve, $W^u(0)$ as a pink curve, and $W^s(q)$ as a cyan curve. Column (a) is for $(a, b, c, \alpha, \beta, \gamma, \mu, \tilde{\mu}) = (0.22, 1, -2, 0.3, 1, 2, 0.004, 0)$, and column (b) is for $(a, b, c, \alpha, \beta, \gamma, \mu, \tilde{\mu}) = (0.22, 1, -2, 0.65, 1, 2, -0.004, 0)$.

We focus our attention on case **B**. It is the next step in understanding a more complicated case, namely, case **C**, and also the main ingredient in the homoclinic-doubling cascade that appears close to bifurcations of higher codimension [16]. As mentioned before, the unfolding of case **B** involves saddle periodic orbits; these have two-dimensional stable and unstable manifolds that may or may not be orientable; this is illustrated in fig. 2 for parameter values close to case **B** for system (2). The first column shows an orientable saddle periodic orbit Γ_o , and the second column a non-orientable (twisted) periodic orbit Γ_t . fig. 2 shows portions of the two-dimensional stable manifolds $W^s(\Gamma_o)$ and $W^s(\Gamma_t)$, and unstable manifolds $W^u(\Gamma_o)$ and $W^u(\Gamma_t)$ of the saddle periodic orbits Γ_o and Γ_t , respectively. The first row shows $W^s(\Gamma_o)$ and $W^s(\Gamma_t)$ as contained in a small tubular neighborhood with radius $d = 0.01$ around Γ_o and Γ_t . The second row shows $W^u(\Gamma_o)$ and $W^u(\Gamma_t)$ in the same corresponding tubular neighborhood. The third row illustrates a larger portion of these manifolds in phase space. Panels (a1) and (a2) illustrate that both $W^s(\Gamma_o)$ and $W^u(\Gamma_o)$ are homeomorphic to a cylinder. In panel (a3), we see that $W^s(\Gamma_o)$ is unbounded but remains a topological cylinder; one side of $W^u(\Gamma_o)$ accumulates on an attracting periodic orbit denoted Γ_o^a and the other side is bounded by $W^u(\mathbf{0})$. Since $W^s(\Gamma_o)$ is unbounded and orientable, it acts as a separatrix that bounds the basin of attraction of Γ_o^a . In contrast, fig. 2 (b1) and (b2) illustrate that $W^s(\Gamma_t)$ and $W^u(\Gamma_t)$ are a topological Möbius band. The non-orientable nature of $W^s(\Gamma_t)$ and $W^u(\Gamma_t)$ is hard to appreciate in panel (b3), but we can see that $W^s(\Gamma_t)$ spirals around the one-dimensional stable manifold $W^s(\mathbf{q})$ of an additional equilibrium denoted \mathbf{q} , and the unstable manifold $W^u(\Gamma_t)$ is bounded by $W^u(\mathbf{0})$.

One of the biggest advantage of using numerical techniques to understand the behaviour of these manifolds is the possibility to study their interactions with other invariant objects and to determine how they can organize phase space; this is shown in fig. 3 for the orientable case in panel (a) and the non-orientable case in panel (b). Here, we also show the two-dimensional stable manifold $W^s(\mathbf{0})$ and the two-dimensional unstable manifold $W^u(\mathbf{q})$ of \mathbf{q} . fig. 3(a) illustrates how $W^s(\mathbf{0})$ spirals towards the topological cylinder formed by $W^s(\Gamma_o)$. Moreover, $W^s(\Gamma_o)$ does not interact with $W^u(\mathbf{q})$, which accumulates onto Γ_o^a ; indeed, $W^u(\mathbf{q})$ lies in the basin of attraction of Γ_o^a and $W^s(\mathbf{0})$ does not. The non-orientable case in fig. 3(b) is quite different, Γ_o^a does not exist and $W^s(\mathbf{0})$ together with $W^s(\Gamma_o)$ rolls around $W^s(\mathbf{q})$. As a consequence, $W^s(\Gamma_t)$ intersects $W^u(\mathbf{q})$ transversally, implying the existence of a heteroclinic orbit from \mathbf{q} to Γ_t .

The main purpose of this paper is to understand how the different manifolds of periodic orbits and equilibria organize the phase space and basins of attraction close to a homoclinic flip bifurcation of case **B**. For this reason, we choose parameter values in each open region of parameter plane, close to the homoclinic flip bifurcation point, to provide representative figures of phase space; here we render each invariant object as in fig. 3 and analyze their transition as a set of parameters is varied. For the purpose of understanding the nature of the basins of attracting periodic orbits, we also provided figures of the intersection sets of the stable manifolds with a suitable sphere. This allows us to describe such basins when parameters are varied. As in case **A**, the existence of an additional saddle focus equilibrium \mathbf{q} in Sandstede's model creates additional dynamics in phase space; these include the existence of a fold curve of (structurally stable) heteroclinic orbits from \mathbf{q} to $\mathbf{0}$ in parameter plane. New for case **B** is that the existence of \mathbf{q} creates regions where there are infinitely many heteroclinic orbits in phase space; these are consequence of structurally stable heteroclinic orbits from \mathbf{q} to Γ_t . We investigate the role and bifurcations of the additional equilibrium \mathbf{q} in system (2). Moreover, we analyze all equilibria in Sandstede's model and consider their bifurcations for parameters close to the homoclinic bifurcation. We find that some equilibria disappear at infinity. Therefore, we utilize *Poincaré compactification* [8, 12, 26] to characterize Sandstede's model at infinity and to complete the bifurcation diagram of these equilibria; see appendix A for details.

The computations in this paper are performed with the software package AUTO [5, 7] and its extension HOMCONT [3]. In particular, the global manifolds are computed with a two-point boundary value problem (2PBVP) set-up; see [2, 21] for details.

The organization of this paper is as follows. In section 2 we introduce notation and background material; here, we also present the parameter values that we use to unfold the two types of homoclinic bifurcations in system (2). In section 2.2.1, we study the bifurcation diagram of the equilibria via a compactified version of system (2). The codimension-two inclination and orbit flip bifurcations for case **B** are the subjects of section 3 and section 4, respectively. section 5 contains the discussion of the results and an outlook for future research. appendix A give a brief summary of Poincaré compactification and an analytic study of system (2) at infinity. Finally, appendix B introduces the 2PBVP-formulations for the computation of a two-dimensional manifold inside a tubular section, and for curves along which the Floquet multipliers of a

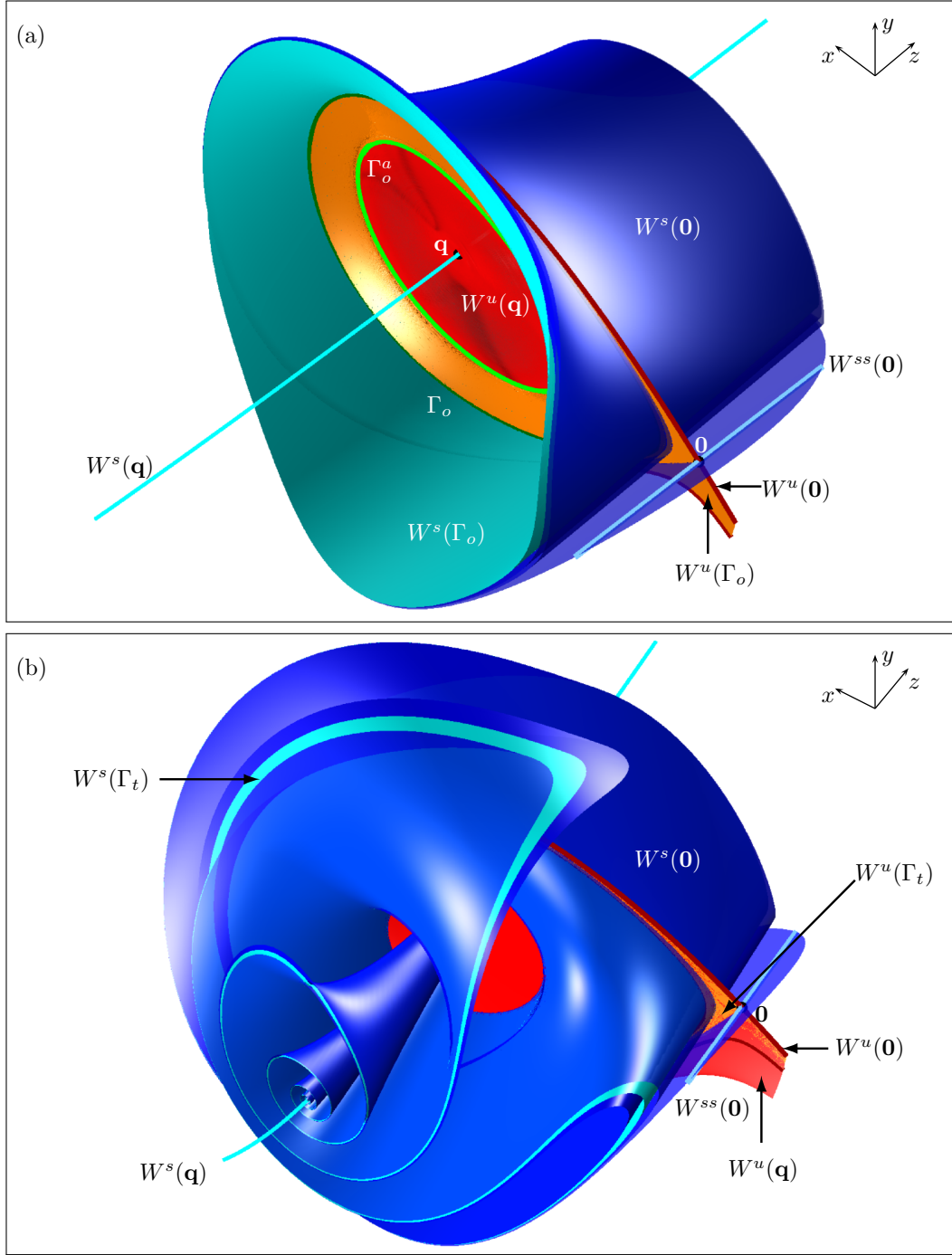


Figure 3: Interaction of the different manifolds of system (2) in \mathbb{R}^3 . Shown are $W^s(0)$ as a dark-blue surface, $W^{ss}(0)$ as a blue curve, $W^u(0)$ as a pink curve, $W^u(q)$ as a red surface, $W^s(q)$ as a cyan curve, $W^s(\Gamma_o)$ and $W^s(\Gamma_t)$ as cyan surfaces, and $W^u(\Gamma_o)$ and $W^u(\Gamma_t)$ as orange surfaces. Panel (a) is for $(a, b, c, \alpha, \beta, \gamma, \mu, \tilde{\mu}) = (0.22, 1, -2, 3, 1, 2, 0.004, 0)$, and panel (b) for $(a, b, c, \alpha, \beta, \gamma, \mu, \tilde{\mu}) = (0.22, 1, -2, 0.65, 1, 2, -0.004, 0)$; compare with fig. 2.

periodic orbit become complex conjugates.

2 Notation and set-up

Recall that we consider system (2) as a representative example of a three-dimensional vector field of the form (1) with a hyperbolic real saddle equilibrium at $\mathbf{0} \in \mathbb{R}^3$. We choose parameters such that the Jacobian $Df(\mathbf{0})$ of $\mathbf{0}$ has two stable and one unstable eigenvalues, $\lambda^{ss} < \lambda^s < 0 < \lambda^u$; we denote by e^{ss} , e^s and e^u the respective associated eigenvectors. The global stable and unstable manifolds of $\mathbf{0}$ are defined as

$$W^s(\mathbf{0}) := \{x \in \mathbb{R}^3 : \phi^t(x) \rightarrow \mathbf{0} \text{ as } t \rightarrow \infty\}, \text{ and} \\ W^u(\mathbf{0}) := \{x \in \mathbb{R}^3 : \phi^t(x) \rightarrow \mathbf{0} \text{ as } t \rightarrow -\infty\}.$$

The Stable Manifold Theorem [33] guarantees that both $W^s(\mathbf{0})$ and $W^u(\mathbf{0})$ are immersed manifolds that are as smooth as f and tangent at $\mathbf{0}$ to the linear eigenspaces $E^s(\mathbf{0}) = \text{span}\{e^s, e^{ss}\}$, and $E^u(\mathbf{0}) = \text{span}\{e^u\}$, respectively. Furthermore, $W^s(\mathbf{0})$ has a one-dimensional strong stable manifold $W^{ss}(\mathbf{0})$, defined as the subset of points on $W^s(\mathbf{0})$ that converge to $\mathbf{0}$ tangentially to e^{ss} .

The stability and invariant manifolds of a periodic orbit Γ of system (2) are defined in a very similar way. We denote its two nontrivial Floquet multipliers by $\Lambda_1, \Lambda_2 \in \mathbb{C}$; they are the eigenvalues of the variational equation along Γ over the period of Γ . Note that there is also the trivial Floquet multiplier 1 associated with the tangent direction of Γ . In a three-dimensional vector field Λ_1 and Λ_2 are always such that their real parts have the same sign; moreover each has an associated eigenfunction that is referred as the Floquet bundle [41].

If $\Lambda_1, \Lambda_2 \in \mathbb{R}$ and $0 < \Lambda_1 < 1 < \Lambda_2$ then one speaks of an orientable saddle periodic orbit, which we denote by Γ_o . Its stable and unstable manifolds $W^s(\Gamma_o)$ and $W^u(\Gamma_o)$, respectively, are locally a cylinder [32, 41]; if $\Lambda_2 < -1 < \Lambda_1 < 0$, then the saddle periodic orbit is non-orientable, denoted Γ_t , and $W^s(\Gamma_t)$ and $W^u(\Gamma_t)$ are locally a Möbius band [32, 41]. The associated stable and unstable manifolds of a saddle periodic orbit are two-dimensional immersed manifolds that are tangent to the Floquet bundle of the periodic orbit associated with Λ_1 and Λ_2 , respectively.

On the other hand, if $\Lambda_1, \Lambda_2 \in \mathbb{C}$ such that $|\Lambda_i| < 1$ for $i = 1, 2$ then we speak of an attracting periodic orbit, which we denote by Γ^a . This implies the existence of an open set $U \subset \mathbb{R}^3$ that satisfies

$$\forall t \geq 0, \phi^t(U) \subset U \text{ and } \bigcap_{t \geq 0} \phi^t(U) = \Gamma^a. \quad (3)$$

Furthermore, the basin of attraction $\mathcal{B}(\Gamma^a)$ of Γ^a is defined as the set of all points in phase space that converge to Γ^a , that is, $\mathcal{B}(\Gamma^a) = \bigcup_{t \geq 0} \phi^t(U)$. If $|\Lambda_1| < |\Lambda_2| < 1$ are both real then we define the strong stable manifold $W^{ss}(\Gamma^a)$ of Γ^a as the set of points that converge to Γ^a tangent to the Floquet bundle associated with Λ_1 ; this strong stable manifold $W^{ss}(\Gamma^a)$ is a two-dimensional immersed manifold. Using the same terminology and notation, we denote the periodic orbit Γ_o^a and its strong stable manifold $W^{ss}(\Gamma_o^a)$ if $0 < \Lambda_1 < \Lambda_2 < 1$ and they are orientable; and as Γ_t^a and $W^{ss}(\Gamma_t^a)$ if $-1 < \Lambda_2 < \Lambda_1 < 0$ and they are non-orientable.

2.1 Homoclinic Flip Bifurcations

Let Γ_{hom} be a homoclinic orbit of $\mathbf{0}$, that is, $\Gamma_{\text{hom}} \subset W^s(\mathbf{0}) \cap W^u(\mathbf{0}) \neq \emptyset$ converges in forward and backward time to $\mathbf{0}$. The homoclinic orbit Γ_{hom} is of codimension one, provided the following conditions hold [15, 20].

- (G1) (Non-resonance) $|\lambda^s| \neq \lambda^u$;
- (G2) (Principal homoclinic orbit) In positive time the homoclinic trajectory approaches the origin tangent to the weakest stable direction e^s ;
- (G3) (Strong inclination) The tangent space $TW^s(\mathbf{0})$ of the stable manifold, followed along Γ_{hom} backward in time, converges to $\text{span}\{e^{ss}, e^u\}$.

For any codimension-one homoclinic orbit, a portion of $W^s(\mathbf{0})$ folds over and closes up along $W^{ss}(\mathbf{0})$; hence, the immersion of $W^s(\mathbf{0})$ in the three-dimensional phase space becomes orientable or non-orientable close to Γ_{hom} ; see panels (a1) and (b1) in fig. 1.

If precisely one of the genericity conditions is not fulfilled then the homoclinic orbit is of codimension two, leading to different kinds of unfoldings. If **(G1)** fails, then one speaks of a *resonant homoclinic bifurcation* [17]. We focus on the inclination flip **(IF)** and orbit flip bifurcations **(OF)** that occur when conditions **(G2)** or **(G3)** fail, respectively. In both cases, one speaks of a homoclinic flip bifurcation, which is of codimension two, if additional genericity conditions are satisfied. Then there exists a curve of homoclinic orbits in any suitable two-parameter plane along which $W^s(\mathbf{0})$ changes from orientable to non-orientable at the codimension-two flip bifurcation point [15, 20].

The unfolding of a flip bifurcation depends on the eigenvalues of $\mathbf{0}$. Three cases have been identified for the inclination flip and the orbit flip bifurcations; they are denoted **A**, **B** and **C**. The unfolding of these cases are topologically the same for both **IF** and **OF** but they satisfy different conditions [18]. More specifically, the eigenvalue conditions and the unfoldings for the respective cases are:

A. If $|\lambda^s| > \lambda^u$ then a single attracting periodic orbit Γ^a is created, for both the orbit flip and inclination flip bifurcations.

B. Suppose the following respective conditions for the inclination and orbit flip bifurcations are satisfied:

- (IF)** $\lambda^u/2 < |\lambda^s| < \lambda^u$ and $|\lambda^{ss}| > \lambda^u$, or
(OF) $|\lambda^s| < \lambda^u$ and $|\lambda^{ss}| > \lambda^u$.

Then the unfolding contains a homoclinic doubling bifurcation, a period-doubling bifurcation and saddle-node bifurcation of periodic orbits.

C. Suppose the following respective conditions for the inclination and orbit flip bifurcation are satisfied:

- (IF)** $|\lambda^s| < \lambda^u$ and $|\lambda^{ss}| < \lambda^u$, or $|\lambda^s| < \lambda^u/2$ and $|\lambda^{ss}| > \lambda^u$, or
(OF) $|\lambda^s| < \lambda^u$ and $|\lambda^{ss}| < \lambda^u$.

Then the unfolding contains k -homoclinic bifurcations [15], for any $k \in \mathbb{N}$, and a region with horseshoe dynamics exists. Two different bifurcation diagrams can arise depending on extra genericity conditions regarding the geometry of the stable manifold $W^s(\mathbf{0})$; details can be found [18].

For both **IF** and **OF**, the unfolding and eigenvalue conditions for cases **A** and **B** were proven for any smooth vector field of dimension $n \geq 3$; see [20, 38]. On the other hand, for case **C** it has been proved that regions of horseshoe dynamics, cascades of period-doubling and homoclinic bifurcations, and strange attractors exist [4, 15, 16, 20, 29, 30]; however, these results have only been proved for three-dimensional vector fields. Moreover, our understanding of the exact nature of the unfoldings of case **C** it is not as complete as cases **A** and **B**.

Since the eigenvalues of an equilibrium depend continuously on the parameters for smooth vector fields, the transitions between cases **A**, **B** and **C**, for both inclination and orbit flip bifurcations, are codimension-three phenomena caused by resonance, that is, a violation of condition **(G1)**; such a resonant homoclinic flip bifurcation was studied in [17] and explored numerically in [31]. Furthermore, in [28] it was shown that C^1 -near a vector field exhibiting an orbit flip of case **C**, there is a vector field with an inclination flip; this approximation result for C^1 -flows provides further insight into the similarities between these two types of flip bifurcations.

We remark that the conditions for the homoclinic flip bifurcation of a hyperbolic equilibrium have been studied for the non-hyperbolic case, namely, for the case of a transcritical bifurcation [24]; the authors show that the non-hyperbolic equilibrium gives rise to new heteroclinic orbits and that its unfolding is different from the hyperbolic case. Reference [11] explores the creation of a *Lorenz-like attractor* in homoclinic loop configurations that exhibit homoclinic flip bifurcations; this happens when two homoclinic orbits connect to the same equilibrium, which in [11] is studied by looking at systems with reflectional symmetry.

2.2 Sandstede's Model

Sandstede [39] introduced a model vector field that exhibits codimension-two flip bifurcations and is particularly suitable for studying their unfoldings. The system has been constructed in such a way that the different cases of both inclination and orbit flip bifurcations occur, and the homoclinic orbits always involve the equilibrium $\mathbf{0}$.

As mentioned in the introduction, we set $\delta = 0$ in the original model introduced in [39], such that the z -axis is invariant. That is, we work with the vector field $X^s(x, y, z)$ as defined by system (2). Note that $\mathbf{0}$ is an equilibrium of X^s for all parameter values; furthermore, since $\delta = 0$ (or if $\mu = 0$), the eigenvalues of $\mathbf{0}$ are given by

$$\lambda_{1,2} = a \pm \sqrt{b^2 + 4\tilde{\mu}^2} \text{ and } \lambda_3 = c,$$

and the eigenvector associated with λ_3 points in the z -direction. Taking into account the parameter ranges found in [31] for **IF** and **OF** of case **B**, we choose the following values for the other parameters:

- (**IF**) For $(a, b, c, \beta, \gamma) = (0.22, 1, -2, 1, 2)$, there is an inclination flip at $(\alpha, \mu, \tilde{\mu}) = (\alpha_B, 0, 0)$ where $\alpha_B \approx 0.4664012$. At this point $\lambda_1 = 1.22$, $\lambda_2 = -0.78$ and $\lambda_3 = -2$. Note that $\lambda^{ss} = \lambda_3$, so for this and nearby parameter values $W^{ss}(\mathbf{0})$ is the z -axis. The codimension-two bifurcation is unfolded by α and μ .
- (**OF**) For $(a, b, c, \beta, \gamma) = (-0.5, 2.5, -1, 0, 0)$, there is an orbit flip at $(\alpha, \mu, \tilde{\mu}) = (1, 0, 0)$. At this point $\lambda_1 = 2$, $\lambda_2 = -3$ and $\lambda_3 = -1$. The codimension-two bifurcation is unfolded by μ and $\tilde{\mu}$.

Note that the choice $\gamma = 2$ for the case **IF** differs from the values taken in [1, 31]. In [1], the value $\gamma = 0$ was used, but for case **B** this value does not give an inclination flip. In [31], the value $\gamma = 3$ was used, but it turns out that the choice $\gamma = 3$ is rather unfortunate with respect to the existence of additional equilibria; we justify our choice of $\gamma = 2$ in the next subsection.

2.2.1 Configuration of Equilibria

We start by determining the equilibria of system (2) and their stability. Because system (2) is a polynomial vector field, we use Poincaré compactification to project the phase space into the three-dimensional open ball $\mathbb{B} := \mathbb{B}^2(2)$ of radius 2. For the compactified model of (2) the sphere $\mathbb{S} := \mathbb{S}^2(2)$ bounding \mathbb{B} represents the dynamics at infinity [12, 26, 27]; appendix A gives more details on the compactification, and shows the respective compactified vector field (8) of system (2) and discusses its behaviour at \mathbb{S} . This compactification allows us to consider all equilibria and continue them with AUTO, even when they interact with infinity.

fig. 4 shows the corresponding bifurcation diagrams of the equilibria of system (2), as determined by using its compactification (8), for both the inclination and orbit flip cases. Specifically, panel (a) shows the inclination flip case **IF** in the (α, γ) -plane of the compactified model (8) for $(a, b, c, \beta, \mu, \tilde{\mu}) = (0.22, 1, -2, 1, 0, 0)$, and panel (b) the orbit flip case **OF** in the $(\tilde{\mu}, \gamma)$ -plane for $(a, b, c, \alpha, \beta, \mu) = (-0.5, 2.5, -1, 1, 0, 0)$. Starting with **IF** in panel (a), we focus on the region near $\gamma = 3$. The origin is always an equilibrium and the squares indicate the number and stability of the additional equilibria. A blue square corresponds to an equilibrium with at least two stable eigenvalues; otherwise the square is red. Squares with a cross refer to saddles and solid squares to sinks (blue) or sources (red). System (2) and its compactification are symmetric under the transformation $(z, \alpha) \rightarrow (-z, -\alpha)$ when $\mu = 0$; hence, there is no need to show the negative values of α in fig. 4. The blue curve represents a saddle-node bifurcation, labeled **SN**, that gives rise to a sink and a saddle; similarly, the red curve **SN** gives rise to a source and a saddle. The line $\gamma = 3$ (brown) represents a degenerate transcritical bifurcation at infinity, labeled **DT** $_{\infty}$. Along the bifurcation curve **DT** $_{\infty}$, an equilibrium reaches infinity, namely, at the non-hyperbolic equilibrium $(0, 0, 2) \in \mathbb{S}$. After the equilibrium crosses the curve **DT** $_{\infty}$, its z -coordinate and all its eigenvalues change sign, that is, it reappears at $(0, 0, -2)$ with the opposite stability. The curves labeled **SN** meet in a degenerate cusp point **DCP** $_{\infty}$ on **DT** $_{\infty}$. The curves **IF** (pink) and **HB** (green) are bifurcations of homoclinic or periodic orbits. Since $\mu = 0$ there exists a homoclinic orbit irrespective of the choices for α and γ [39]. The homoclinic orbit is orientable for small α and changes type at the inclination flip curve **IF**, which is the pink curve; the homoclinic orbit is non-orientable for values of α to the right of **IF**. The Hopf bifurcation **HB** gives rise to an orientable attracting periodic orbit Γ_0^a that merges with the orientable homoclinic orbit and disappears in the homoclinic flip bifurcation **IF**.

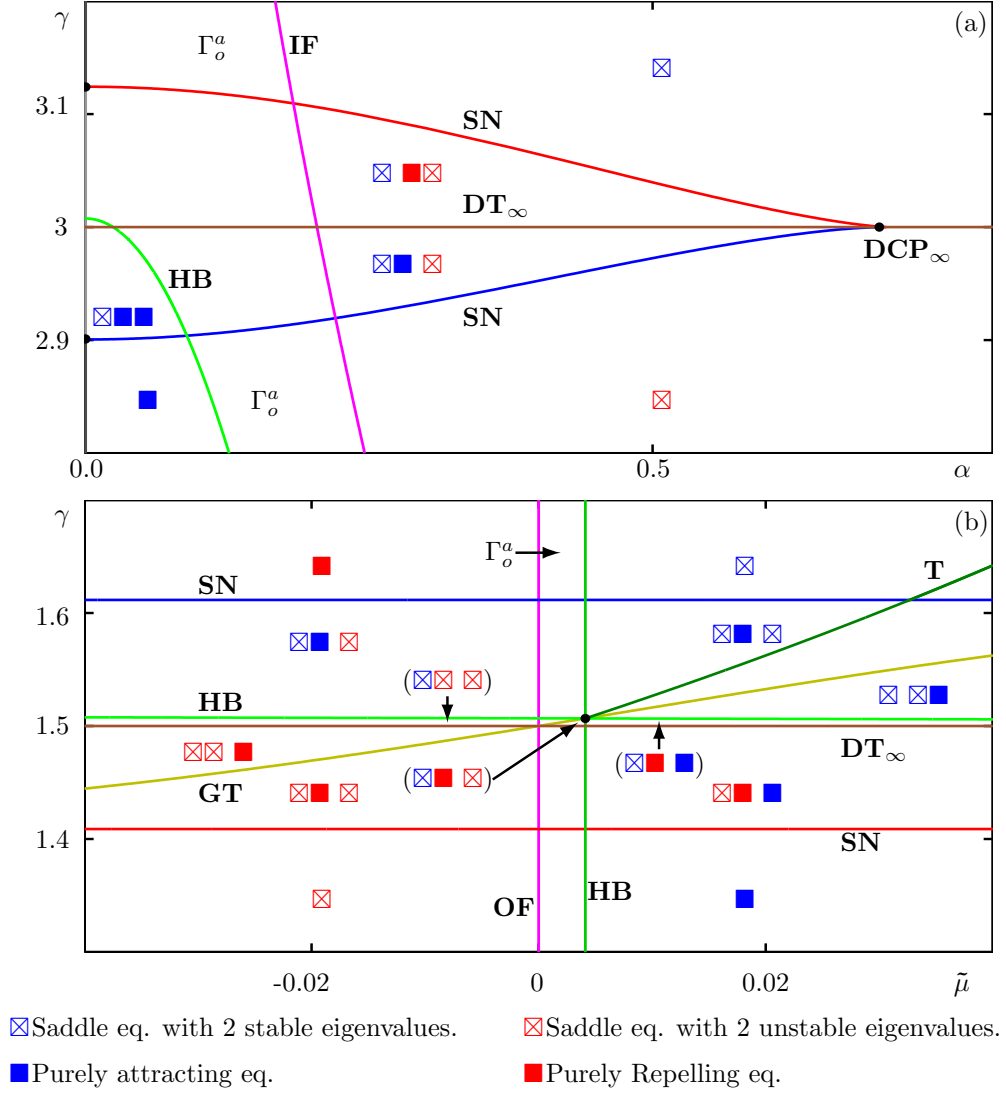


Figure 4: Bifurcation diagram of equilibria for system (2). Panel (a) shows the (α, γ) -plane with $(a, b, c, \beta, \mu, \tilde{\mu}) = (0.22, 1, -2, 1, 0, 0)$ and panel (b) the $(\tilde{\mu}, \gamma)$ -plane with $(a, b, c, \alpha, \beta, \mu) = (-0.5, 2.5, -1, 1, 0, 0)$. Each equilibrium is represented by a square, where color and filling indicates its eigenvalue configuration as explained in the legend. Shown are saddle-node bifurcations **SN** as red and blue curves, inclination flip **IF** and orbit flip bifurcations **OF** as pink curves, Hopf bifurcation **HB** as a light-green curve, torus bifurcation **T** as a dark-green curve, transcritical bifurcation **GT** as a yellow curve, and non-generic transcritical bifurcation at infinity **DT $_{\infty}$** as a brown curve; the point **DCP $_{\infty}$** is a nongeneric cusp point at infinity. An attracting periodic orbit Γ_o^a exist between **HB** and **IF** in panel (a), and between **HB** and **OF** in panel (b).

We choose to focus on the same situation that was studied in [1], namely, where there is a single extra saddle-focus equilibrium $\mathbf{q} \in \mathbb{R}^3$, with a two-dimensional unstable manifold $W^u(\mathbf{q})$ and a one-dimensional stable manifold $W^s(\mathbf{q})$. For this reason, we fix $\gamma = 2$ and vary $\alpha > 0$, which is equivalent to the situation shown along the horizontal line $\gamma = 2.8$ in fig. 4(a).

fig. 4(b) shows that there is a similar configuration of equilibria for parameters $\tilde{\mu}$ and γ for the **OF** case. We again find a degenerate transcritical bifurcation **DT**_∞ at infinity at $\gamma = 1.5$, two curves of Hopf bifurcation **HB** and two saddle-node bifurcation curves **SN**. We also find a curve of torus bifurcation **T** (dark-green curve) and a generic transcritical bifurcation **GT** (light-green). There exists a curve **OF** of orbit flip bifurcations at $\tilde{\mu} = 0$ in the $(\tilde{\mu}, \gamma)$ -plane. However, the homoclinic orbit that goes through these orbit flip bifurcations cannot be found in this parameter plane.

For the case **OF**, we again consider the situation where system (2) has an additional equilibrium \mathbf{q} with the same properties as described before. For this reason, we can study the orbit flip bifurcation by setting $\gamma = 0$, which is equivalent to the horizontal line $\gamma = 1.3$ in fig. 4(b).

3 Inclination flip of case B

We denote the inclination flip **IF** of type **B** by **B_I**. On the level of the codimension-one homoclinic bifurcation, **B_I** marks the transition from an orientable homoclinic bifurcation to a non-orientable one by breaking condition **(G3)**. fig. 5 shows the unfolding of **B_I** in the (α, μ) -plane for system (2) with the other parameters as stated in section 2.2. The bifurcation curves that emanate from the codimension-two point are a codimension-one orientable homoclinic bifurcation **H_o** (brown curve), a codimension-one non-orientable homoclinic bifurcation **H_t** (brown curve), a saddle-node bifurcation of periodic orbits **SNP** (cyan curve), a period-doubling bifurcation **PD** (red curve) and a codimension-one homoclinic bifurcation **²H_o** (blue curve), as proven in [20]. We also find an additional curve of fold bifurcation of heteroclinic orbits **F** and curves **CC**[±] (purple curves) that represent the moment that the Floquet multipliers of an attracting periodic orbit becomes complex conjugates. These curves divide the (α, μ) -plane in to open regions, which are labeled by red numbers. Even though the curves **CC**[±] are not bifurcation curves, they bound region **1*** in fig. 5 where the Floquet multipliers of Γ^a are complex conjugates. Crossing through **CC**[±] and this region results in the transition of Γ^a having a non-orientable to having an orientable strong stable manifold, so that this attracting periodic orbit can bifurcate at the curves **SNP** and **PD**, respectively.

Starting from region **1**, where an orientable attracting periodic orbit Γ_o^a exists, we move to region **2** through **H_o**. This homoclinic orbit creates an orientable saddle periodic orbit Γ_o in region **2**, which disappears with Γ_o^a in the **SNP** bifurcation as we cross in to region **3**. The transition between regions **3** and **4** is the **H_t** bifurcation. As in region **2**, the homoclinic orbit becomes a saddle periodic orbit Γ_t in region **4**, but this saddle periodic orbit is non-orientable. As we move to region **5**, the periodic orbit Γ_t undergoes the **PD** bifurcation and becomes the non-orientable attracting periodic orbit Γ_t^a ; furthermore, an orientable saddle periodic orbit ${}^2\Gamma_o$ with twice the period of Γ_t is created. Next, the transition between regions **5** and **6** is characterized by the disappearance of ${}^2\Gamma_o$ in **²H_o** (blue curve) as it becomes an homoclinic orbit. As shown in fig. 5. The curve **F** delimits region **6** and marks the creation of a pair of heteroclinic orbits from \mathbf{q} to $\mathbf{0}$ that exists in regions **4**, **5** and **6**. These heteroclinic orbits represent the transverse intersection between $W^s(\mathbf{0})$ and $W^u(\mathbf{q})$, which becomes tangent at **F** so that the two heteroclinic orbits merge and then disappear in region **1'**. Region **1'** is topologically equivalent to region **1** but the attracting periodic orbit Γ_t^a is non-orientable instead of orientable for Γ_o^a in region **1**. The transition from region **1'** to region **1** occurs via a crossing of the curves **CC**[−] and **CC**⁺ where the Floquet multipliers of Γ_t^a (Γ_o^a) in region **1'** (**1**) change from being real positive (negative) to complex conjugate. In region **1***, bounded by **CC**⁺ and **CC**[−], the periodic orbit does not have a strong stable manifold. appendix B gives details on the computation of the curves **F**, **CC**⁺ and **CC**[−].

Our goal is now to characterize the topological properties of the global manifolds in a neighborhood of the inclination flip bifurcation. We use the bifurcation diagram in fig. 5 as a reference to describe the changes in the organization of the manifolds of system (2) in phase space, as α and μ vary between the different regions in the (α, μ) -plane. table 1 provides an overview of the representative values of α and μ we selected from each region. We also illustrate the manifolds for representative parameter points approximately on **H_o**, **H_t**, **²H_o**, **F** and at **B_I**; these values are given in table 2. We first present their phase portrait in \mathbb{R}^3 , where the

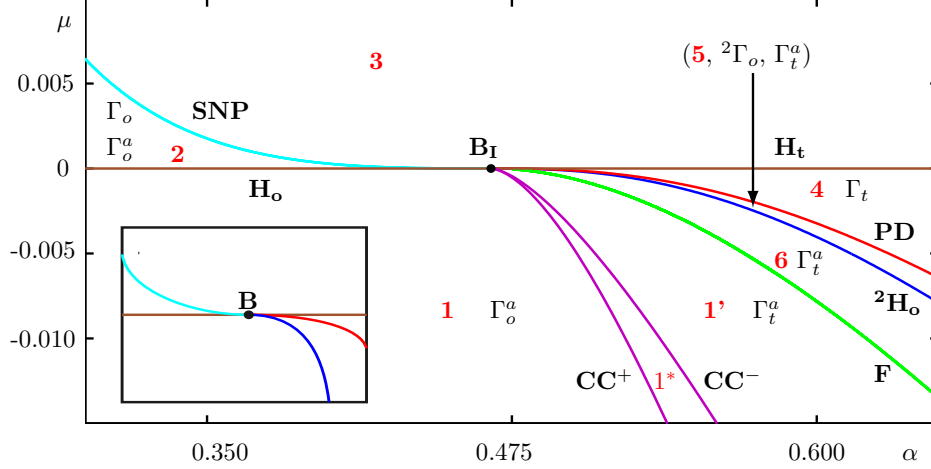


Figure 5: Bifurcation diagram in the (α, μ) -plane near an inclination flip bifurcation $\mathbf{B_I}$ of system (2) for other parameters as given in section 2.2. The inset shows only the curves of the theoretical unfolding of case **B** [20]. Shown are the homoclinic bifurcations $\mathbf{H_o}$ and $\mathbf{H_t}$ as brown curves, the homoclinic bifurcation ${}^2\mathbf{H_o}$ as a blue curve, the saddle-node bifurcation **SNP** of periodic orbit as a cyan curve, the period doubling bifurcation **PD** as a red curve, the fold bifurcation **F** of heteroclinic orbits as green curve, and the loci \mathbf{CC}^\pm as purple curves.

Region	1	2	3	4	5	6	1'
α	0.300	0.300	0.650	0.650	0.650	0.650	0.650
μ	-0.004	0.004	0.004	-0.004	-0.007	-0.010	-0.014

Table 1: Chosen representative parameter values for the different open regions in fig. 5.

Curve	$\mathbf{H_o}$	$\mathbf{B_I}$	$\mathbf{H_t}$	${}^2\mathbf{H_o}$	F
α	0.3000000	0.4664012	0.6500000	0.6500000	0.6500000
μ	0	0	0	-0.0079047	-0.0134990

Table 2: Chosen representative parameter values at selected bifurcations in fig. 5.

orbit segments that forms the two-dimensional stable (unstable) manifolds are computed by restricting one end point to lie in the sphere $\mathbb{S}^* := \{x \in \mathbb{R}^3 : \|x - c\| = R\}$ with $c := (c_x, c_y, c_z) = (0.5, 0, 0)$ and $R = 0.6$.

3.1 Manifolds in the open regions near $\mathbf{B_I}$

fig. 6 shows phase portraits in each region and at the bifurcations ${}^2\mathbf{H_o}$ and **F**. Specifically, we show the equilibria $\mathbf{0}$ and \mathbf{q} along with their stable and unstable manifolds, as well as the periodic orbits and their manifolds when they exist. In the following, we cycle around $\mathbf{B_I}$ through the bifurcation diagram in fig. 5, starting from region **1**, and describe the transitions on the level of the invariant manifolds in phase space. To improve clarity and understanding of fig. 6, the accompanying animations ([GKO_Bflip_animatedFig6-1.gif](#)) and ([GKO_Bflip_animatedFig6-2.gif](#)), show the respective objects rotating clockwise around the y -axis.

3.1.1 Manifolds in region 1

Region **1** is characterized by the existence of an orientable attracting periodic orbit Γ_o^a . The corresponding phase portrait in panel **1** of fig. 6 shows how one branch of $W^u(\mathbf{0})$ (red curve) spirals towards Γ_o^a (green curve). The two-dimensional stable manifold $W^s(\mathbf{0})$ (blue surface) folds over $W^u(\mathbf{0})$ and trajectories on $W^s(\mathbf{0})$ escape towards infinity in backward time. Furthermore, the two-dimensional unstable manifold $W^u(\mathbf{q})$ (red surface)

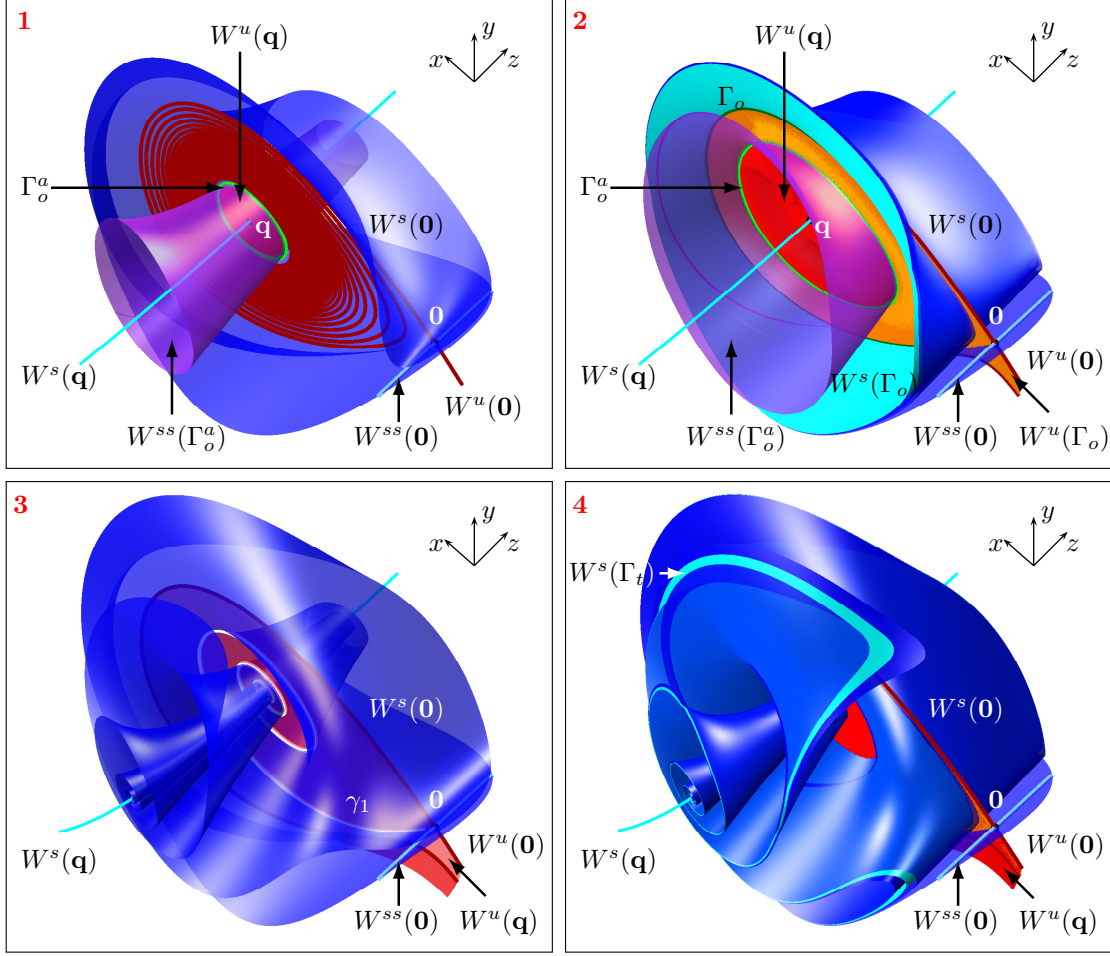


Figure 6: Phase portraits of system (2) in the different regions **1-6** and at the bifurcations \mathbf{H}_o and \mathbf{F} of the (α, μ) -plane in fig. 5. Shown are $W^s(\mathbf{0})$ as a dark-blue surface, $W^{ss}(\mathbf{0})$ as a blue curve, $W^u(\mathbf{0})$ as a pink curve, $W^u(\mathbf{q})$ as a red surface, $W^s(\mathbf{q})$ as a cyan curve, $W^s(\Gamma_o)$ and $W^s(\Gamma_t)$ as cyan surfaces, $W^u(\Gamma_o)$ and $W^u(\Gamma_t)$ as orange surfaces, and $W^{ss}(\Gamma_t^a)$ and $W^{ss}(\Gamma_o^a)$ as purple surfaces. The (α, μ) -values for each panel are given in table 1 and table 2. See also the accompanying animation ([GKO_Bflip_animatedFig6-1.gif](#)).

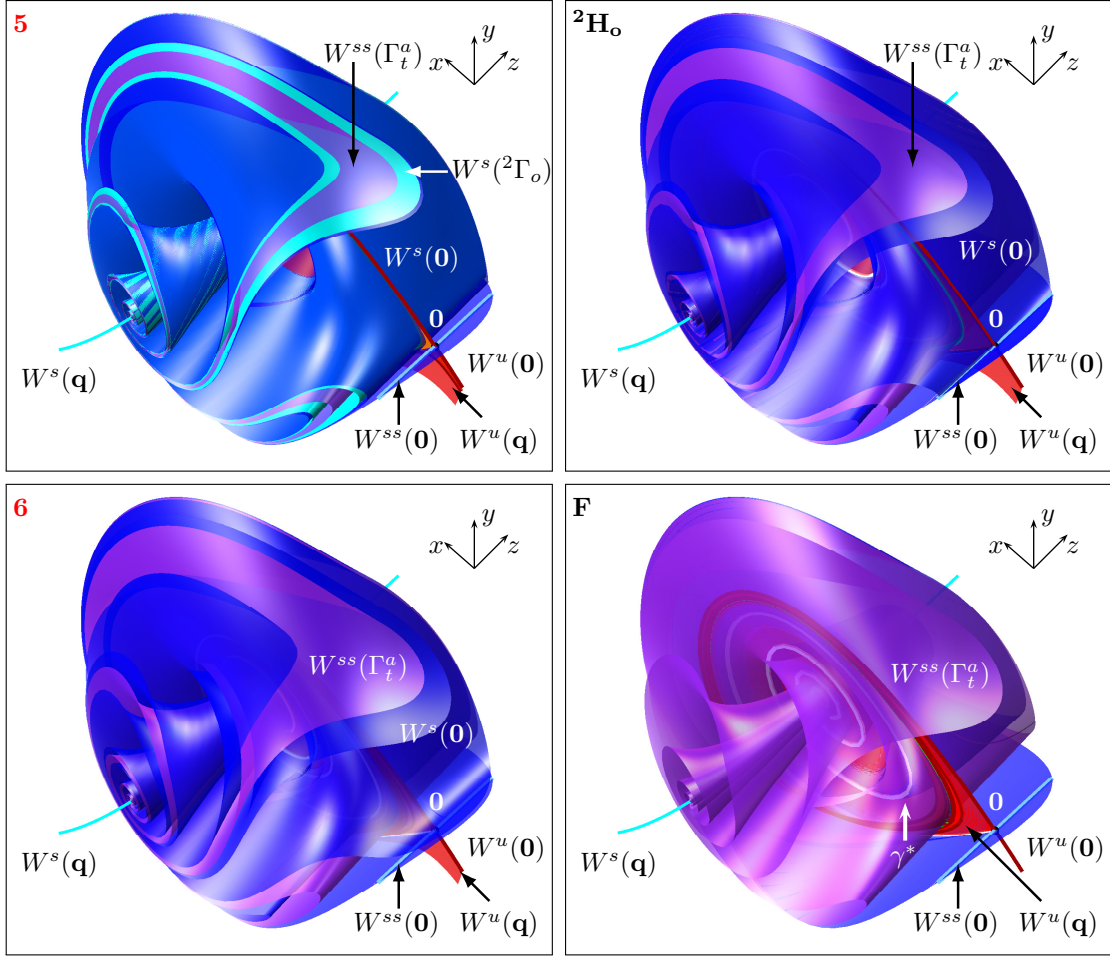


Figure 6: Continued. See also the accompanying animation ([GKO_Bflip_animatedFig6-2.gif](#)).

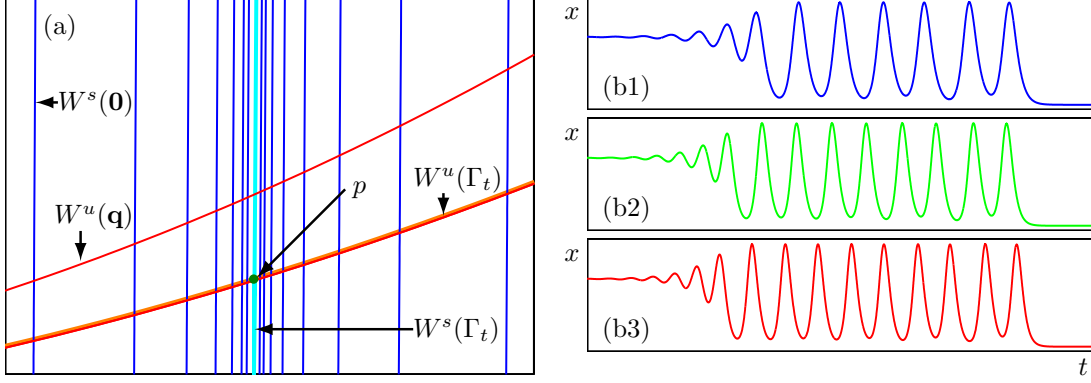


Figure 7: Intersection of global manifolds in region 4. Panel (a) shows the intersections of the manifolds with the plane Σ ; points in Σ have the same y -coordinate as \mathbf{q} . Shown are $W^s(\mathbf{0})$ as blue curves, $W^s(\Gamma_o)$ as a cyan curve, $W^u(\Gamma_t)$ as an orange curve, $W^u(\mathbf{q})$ as red curves and the point $p \in \Gamma_t \cap \Sigma$ as a green dot. Panel (b) shows (scaled) time series in x of representative heteroclinic orbits from \mathbf{q} to $\mathbf{0}$, respectively.

accumulates on Γ_o^a . In fact, Γ_o^a is the boundary of $W^u(\mathbf{q})$. Since the Floquet multipliers of Γ_o^a are positive, its strong stable manifold $W^{ss}(\Gamma_o^a)$ (purple surface) is a topological cylinder. We note that the one-dimensional stable manifold $W^s(\mathbf{q})$ (cyan curve) lies in the interior of $W^{ss}(\Gamma_o^a)$. Therefore, none of the other stable manifolds outside of $W^{ss}(\Gamma_o^a)$ can accumulate onto $W^s(\mathbf{q})$ in backward time.

3.1.2 Manifolds in region 2

The bifurcation curve \mathbf{H}_o , between region 1 and 2, creates the homoclinic orbit Γ_{hom} . As we transition to region 2, the orbit Γ_{hom} becomes the orientable saddle periodic orbit Γ_o (dark-green curve) in panel 2 of fig. 6. It has two-dimensional stable and unstable manifolds $W^s(\Gamma_o)$ (cyan surface) and $W^u(\Gamma_o)$ (orange surface), respectively. Since Γ_o is an orientable saddle periodic orbit, both $W^s(\Gamma_o)$ and $W^u(\Gamma_o)$ are orientable, but $W^u(\Gamma_o)$ is bounded by Γ_o^a and $W^u(\mathbf{0})$, while $W^s(\Gamma_o)$ is unbounded. As shown in panel 2 of fig. 6, the one-dimensional manifold $W^u(\mathbf{0})$ no longer accumulates on Γ_o^a , but one branch folds over $W^s(\mathbf{0})$ before both branches move off to infinity. Furthermore, $W^s(\mathbf{0})$ now accumulates (in backward time) onto $W^s(\Gamma_o)$. Note that $W^s(\mathbf{0})$ intersects $W^u(\Gamma_o)$ transversally; this implies the existence of a heteroclinic cycle-to-point connecting orbit from Γ_o to $\mathbf{0}$, which exists in the open region 2 in fig. 5.

3.1.3 Manifolds in region 3

The transition between regions 2 and 3 occurs at the saddle-node bifurcation of periodic orbits **SNP**. At **SNP**, the periodic orbits Γ_o , Γ_o^a and their manifolds $W^s(\Gamma_o)$ and $W^{ss}(\Gamma_o^a)$ merge, and disappear as we transition in to region 3. Consequently, $W^s(\mathbf{0})$ now spirals towards \mathbf{q} and accumulates on $W^s(\mathbf{q})$ in backward time; see panel 3 of fig. 6. The manifold $W^u(\mathbf{0})$ is now the boundary of $W^u(\mathbf{q})$ and the manifolds $W^s(\mathbf{0})$ and $W^u(\mathbf{q})$ intersect transversally in region 3; this implies the existence of a heteroclinic orbit γ_1 (white curve) from \mathbf{q} to $\mathbf{0}$.

3.1.4 Manifolds in region 4

Regions 3 and 4 are separated by a curve \mathbf{H}_t of codimension-one non-orientable homoclinic bifurcations. The homoclinic orbit Γ_{hom} becomes the non-orientable saddle periodic orbit Γ_t in region 4. The stable manifold $W^s(\mathbf{0})$ accumulates onto $W^s(\Gamma_t)$ (cyan surface) in backward time. In contrast to region 2, the non-orientable stable manifold $W^s(\Gamma_t)$ is not a separatrix but spirals towards \mathbf{q} and accumulates in backward time onto $W^s(\mathbf{q})$. Furthermore, we see intersections between the different manifolds in region 4, although it is hard to appreciate their structure.

To illustrate the nature of these manifold interactions we consider their intersection sets with the plane $\Sigma := \{(x, y, z) \in \mathbb{R}^3 : y = \mathbf{q}_y\}$, where \mathbf{q}_y is the y -component of \mathbf{q} . fig. 7(a) shows the intersection sets of

$W^s(\mathbf{0})$, $W^u(\mathbf{q})$, $W^s(\Gamma_t)$ and $W^u(\Gamma_t)$ with Σ in a neighborhood of one of the two points $p \in \Gamma_t \cap \Sigma$. Locally near p , there is a single curve (cyan) representing $W^s(\Gamma_t) \cap \Sigma$ and another single curve (orange) representing $W^u(\Gamma_t) \cap \Sigma$. Since $W^u(\mathbf{q}) \cap \Sigma$ intersects $W^s(\Gamma_t) \cap \Sigma$ and $W^u(\Gamma_t) \cap \Sigma$ intersects $W^s(\mathbf{0}) \cap \Sigma$, there exist structurally stable heteroclinic orbits from \mathbf{q} to Γ_t and from Γ_t to $\mathbf{0}$, respectively. As a consequence of the λ -lemma [33, 46], the intersection sets $W^s(\mathbf{0}) \cap \Sigma$ (blue) and $W^u(\mathbf{q}) \cap \Sigma$ (red) give rise to several curves in the neighborhood of p that accumulate onto $W^s(\Gamma_t) \cap \Sigma$ and $W^u(\Gamma_t) \cap \Sigma$, respectively. Therefore, there exist transversal intersections between the sets $W^u(\mathbf{q}) \cap \Sigma$ and $W^s(\mathbf{0}) \cap \Sigma$, which imply the existence of structurally stable heteroclinic orbits from \mathbf{q} to $\mathbf{0}$. Panels (b1)–(b3) of fig. 7 show the evolution of the x -variable with respect to time for three heteroclinic orbits from \mathbf{q} to $\mathbf{0}$ in region 4; observe how they differ in the number of big excursions before converging to $\mathbf{0}$, these excursions correspond to intersection points in Σ close to p . The λ -lemma guarantees the sets $W^u(\mathbf{q}) \cap \Sigma$ and $W^s(\mathbf{0}) \cap \Sigma$ intersect in *an arbitrary small neighborhood* of p ; therefore there exist infinitely many intersection points. Only a finite number of these intersection points corresponds to a single heteroclinic orbit from \mathbf{q} to $\mathbf{0}$; hence, there are indeed infinitely many heteroclinic orbits from \mathbf{q} to $\mathbf{0}$ in region 4.

We remark that the manifolds $W^u(\mathbf{q})$ and $W^s(\mathbf{0})$ shown in panel 4 of fig. 6 are only computed up to the first two of their infinitely many layers that intersect \mathbb{S}^* ; hence, the accumulation of these manifold with the respective invariant manifolds of Γ_o is not visible in panel 4 of fig. 6.

3.1.5 Manifolds in region 5

When crossing from region 4 to region 5 a period-doubling bifurcation **PD** occurs. The saddle periodic orbit Γ_t becomes a non-orientable attracting periodic orbit Γ_t^a , and an orientable saddle periodic orbit ${}^2\Gamma_o$ with twice the period of Γ_t^a emanates from the period-doubling bifurcation into region 5.

Panel 5 in fig. 6 shows that $W^s({}^2\Gamma_o)$ (cyan) and $W^s(\mathbf{0})$ accumulate onto \mathbf{q} and $W^s(\mathbf{q})$ in backward time. The periodic orbit Γ_t^a is attracting in region 5, but its strong stable manifold $W^{ss}(\Gamma_t^a)$ (purple) can be viewed as the continuation of $W^s(\Gamma_t)$. The portion of $W^{ss}(\Gamma_t^a)$ relative to $W^s({}^2\Gamma_o)$ suggests that the basin of attraction $\mathcal{B}(\Gamma_t^a)$ of Γ_t^a is bounded by $W^s({}^2\Gamma_o)$. Indeed, one side of $W^u({}^2\Gamma_o)$ accumulates onto Γ_t^a , while the other side intersects $W^s(\mathbf{0})$. Hence, the situation is very similar to that in region 4: there exists one transversal heteroclinic orbit from ${}^2\Gamma_o$ to $\mathbf{0}$, and there exist infinitely many heteroclinic orbits from \mathbf{q} to $\mathbf{0}$. Furthermore, a two-dimensional submanifold of $W^u(\mathbf{q})$ lies in the open set $\mathcal{B}(\Gamma_t^a)$; hence this submanifold accumulates on Γ_t^a and its boundary corresponds to an intersection of $W^u(\mathbf{q})$ and $W^s({}^2\Gamma_o)$, that is, there exist transversal heteroclinic orbits from \mathbf{q} to ${}^2\Gamma_o$. Also, as in region 4, the one-dimensional unstable manifold $W^u(\mathbf{0})$ is contained in part of the closure of both $W^u({}^2\Gamma_o)$ and $W^u(\mathbf{q})$.

3.1.6 Manifolds in region 6

The boundary between region 5 to 6 is the curve ${}^2\mathbf{H}_o$ of codimension-one orientable homoclinic bifurcation. The moment of the homoclinic bifurcation is illustrated in panel ${}^2\mathbf{H}_o$ of fig. 6. The limit of the saddle periodic orbit ${}^2\Gamma_o$ is the orientable codimension-one homoclinic orbit ${}^2\Gamma_{\text{hom}}$ at ${}^2\mathbf{H}_o$. Note that ${}^2\Gamma_o$ and its manifolds have disappeared, and so have the heteroclinic orbits connecting ${}^2\Gamma_o$ with $\mathbf{0}$ and \mathbf{q} . Hence there are no longer infinitely many codimension-zero heteroclinic orbits from \mathbf{q} to $\mathbf{0}$. We find that $W^s(\mathbf{0})$ interacts non-trivially with $W^u(\mathbf{q})$ in two transversal heteroclinic orbits from \mathbf{q} to $\mathbf{0}$ that persist through the homoclinic bifurcation ${}^2\mathbf{H}_o$. They bound the two-dimensional submanifold $W^u(\mathbf{q})$ that accumulates on Γ_t^a . Since these two heteroclinic orbits can be viewed as the continuation of the two heteroclinic orbits from \mathbf{q} to ${}^2\Gamma_o$ in region 5. The other infinitely many heteroclinic orbits from \mathbf{q} to $\mathbf{0}$ all disappear at once in the homoclinic bifurcation ${}^2\mathbf{H}_o$.

The homoclinic orbit ${}^2\Gamma_{\text{hom}}$ disappears but the non-orientable attracting periodic orbit Γ_t^a and the two transversal heteroclinic orbits from \mathbf{q} to $\mathbf{0}$ persist in region 6. In particular, these two heteroclinic orbits still bound the portion of $W^u(\mathbf{q})$ that is attracted by Γ_t^a . Note that the branch of $W^u(\mathbf{0})$ that formed ${}^2\Gamma_{\text{hom}}$ now spirals towards Γ_t^a . It is worth noting that the phase space in region 6 is topologically equivalent to that of region 3 for case **A** in [1].

3.1.7 Manifolds in region 1'

At the curve **F**, which is the transition from region **6** to region **1'**, the two-dimensional manifolds $W^s(\mathbf{0})$ and $W^u(\mathbf{q})$ lose their two intersection orbits in a quadratic tangency; see panel **F** of fig. 6. Hence, the two heteroclinic orbits merge to become the heteroclinic orbit γ^* , representing the last moment where $W^u(\mathbf{0})$ is part of the boundary of $W^u(\mathbf{q})$.

In region **1'**, the manifolds $W^s(\mathbf{0})$ and $W^u(\mathbf{q})$ do no longer interact with each other, and $W^u(\mathbf{q})$ accumulates entirely on Γ_t^a . The nontrivial Floquet multipliers of Γ_t^a in region **1'** become equal at the curve **CC**⁻; they are then complex conjugates with negative real part close to **CC**⁻ in region **1***. Hence, there is not a well-defined strong stable manifold of Γ^a in region **1***. As we approached region **1** from region **1***, the Floquet multipliers of Γ^a cross the imaginary axis and become complex conjugates with positive real part close to the curve **CC**⁺. At this curve, the non-trivial Floquet multipliers are both the same positive real number. They then become two distinct positive real values in region **1**, so that Γ_o^a has a well-defined strong stable manifold again. This transition through **CC**⁻ and **CC**⁺ allows the twisted periodic orbit Γ_t^a to become the orientable Γ_o^a that then disappears with Γ_o at the bifurcation **SNP** [32]. Our numerical computations indicate that the two curves **CC**⁺ and **CC**⁻ are not tangent to the homoclinic bifurcation curve at **B**_I but approach this codimension-two point at a non-zero angle; see fig. 5. Since the manifolds in regions **1'** and **1*** are qualitatively the same as in region **1**, except for the properties of the strong stable manifold $W^{ss}(\Gamma^a)$, we do not show the respective phase portraits in fig. 6.

3.2 Intersections of the invariant manifolds with a sphere

It is a challenge to extract the precise nature of the phase portraits in the panels of fig. 6 in terms of the re-organization of the basins of attracting periodic orbits. Therefore, we now study the intersection sets of the respective invariant manifolds with the sphere \mathbb{S}^* of radius $R = 0.6$ centered at $c = (c_x, c_y, c_z) = (0.5, 0, 0)$. Since \mathbb{S}^* is a compact set, all intersection sets of the manifolds of system (2) must be bounded. We consider the intersection sets:

$$\begin{aligned} \widehat{W}^s(\mathbf{0}) &:= W^s(\mathbf{0}) \cap \mathbb{S}^*, \quad \widehat{W}^{ss}(\mathbf{0}) := W^{ss}(\mathbf{0}) \cap \mathbb{S}^*, \quad \widehat{W}^s(\mathbf{q}) := W^s(\mathbf{q}) \cap \mathbb{S}^*, \\ \widehat{W}^s(\Gamma_o^a) &:= W^s(\Gamma_o^a) \cap \mathbb{S}^*, \quad \widehat{W}^s(\Gamma_t^a) := W^s(\Gamma_t^a) \cap \mathbb{S}^* \text{ and } \widehat{W}^{ss}(\Gamma_{o/t}^a) := W^{ss}(\Gamma_{o/t}^a) \cap \mathbb{S}^*. \end{aligned}$$

In particular, the intersection sets of all two-dimensional manifolds that are transverse to \mathbb{S}^* are curves, while the one-dimensional manifolds intersect \mathbb{S}^* in points. We also determine the regions on \mathbb{S}^* that correspond to the intersection sets of the basin of attraction $\mathcal{B}(\Gamma^a)$ of Γ^a ; we denote this set $\widehat{\mathcal{B}}(\Gamma^a)$ and color it yellow in the subsequent figures.

It is convenient to represent these intersection sets in the plane; to this end, we use stereographic projection onto the (x, z) -plane via the transformation

$$(x', y', z') \in \mathbb{S}^* \mapsto \left(\frac{R(x' - c_x)}{R + (y' - c_y)}, \frac{R(z' - c_z)}{R + (y' - c_y)} \right) \in \mathbb{R}^2. \quad (4)$$

This transformation translates c to **0**, and then projects a point on the (translated) sphere \mathbb{S}^* along the line through $(0, -R, 0)$ to a point on the tangent plane of the sphere at $(0, R, 0)$, that is, the plane parallel to the (x, z) -plane through $(0, R, 0)$. fig. 8 shows the intersection sets with \mathbb{S}^* in each region close to the inclination flip. As in the previous section, fig. 8 starts with the situation for region **1** and cycles through the bifurcation diagram of the inclination flip bifurcation. However, now we show also the situation at region **1'**. The left column of fig. 8 shows stereographic projections of the intersections sets of the manifolds in each region close to the inclination flip as computed with AUTO [5, 7]. The right column shows topological sketches of these projections to illustrate and accentuate important features.

3.2.1 Intersection sets in regions 1 to 3

In region **1** the intersection set $\widehat{W}^s(\mathbf{0})$ (blue curve) on \mathbb{S}^* is a single closed curve; due to the fact that $W^s(\mathbf{0})$ is a topological cylinder. The region enclosed by $\widehat{W}^s(\mathbf{0})$ contains the two points of $\widehat{W}^s(\mathbf{q})$ (dark blue). The orientable attracting periodic orbit Γ_o^a that exists in region **1** does not intersect \mathbb{S}^* . Moreover, the intersection

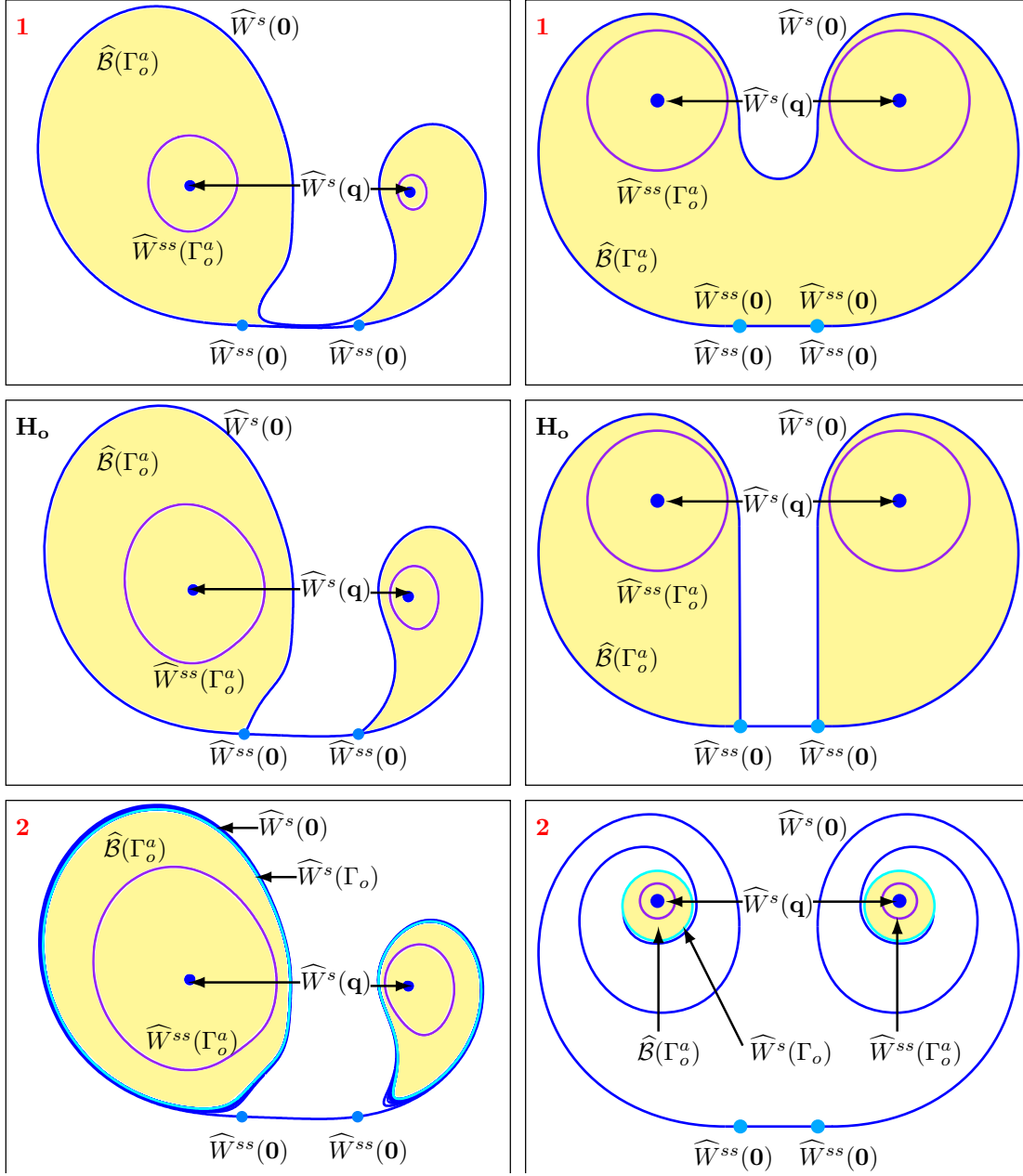


Figure 8: Stereographic projections of the intersection sets of the invariant manifolds with \mathbb{S}^* in the regions and at bifurcations of the bifurcation diagram in fig. 5 near the inclination flip $\mathbf{B_I}$; the first column shows the computed manifolds of system (2) and the second column are topological sketches. Shown are $\hat{W}^s(0)$ as dark-blue curves, $\hat{W}^{ss}(0)$ as light-blue dots and $\hat{W}^s(q)$ dark-blue dots, $\hat{W}^s(\Gamma_o)$, $W^s(2\Gamma_o)$ and $\hat{W}^s(\Gamma_t)$ as cyan curves, $\hat{W}^{ss}(\Gamma_{o/t}^a)$ as purple curves and $\hat{\mathcal{B}}(\Gamma_{o/t}^a)$ as a shaded yellow region. For respective parameter values see table 1 and table 2.

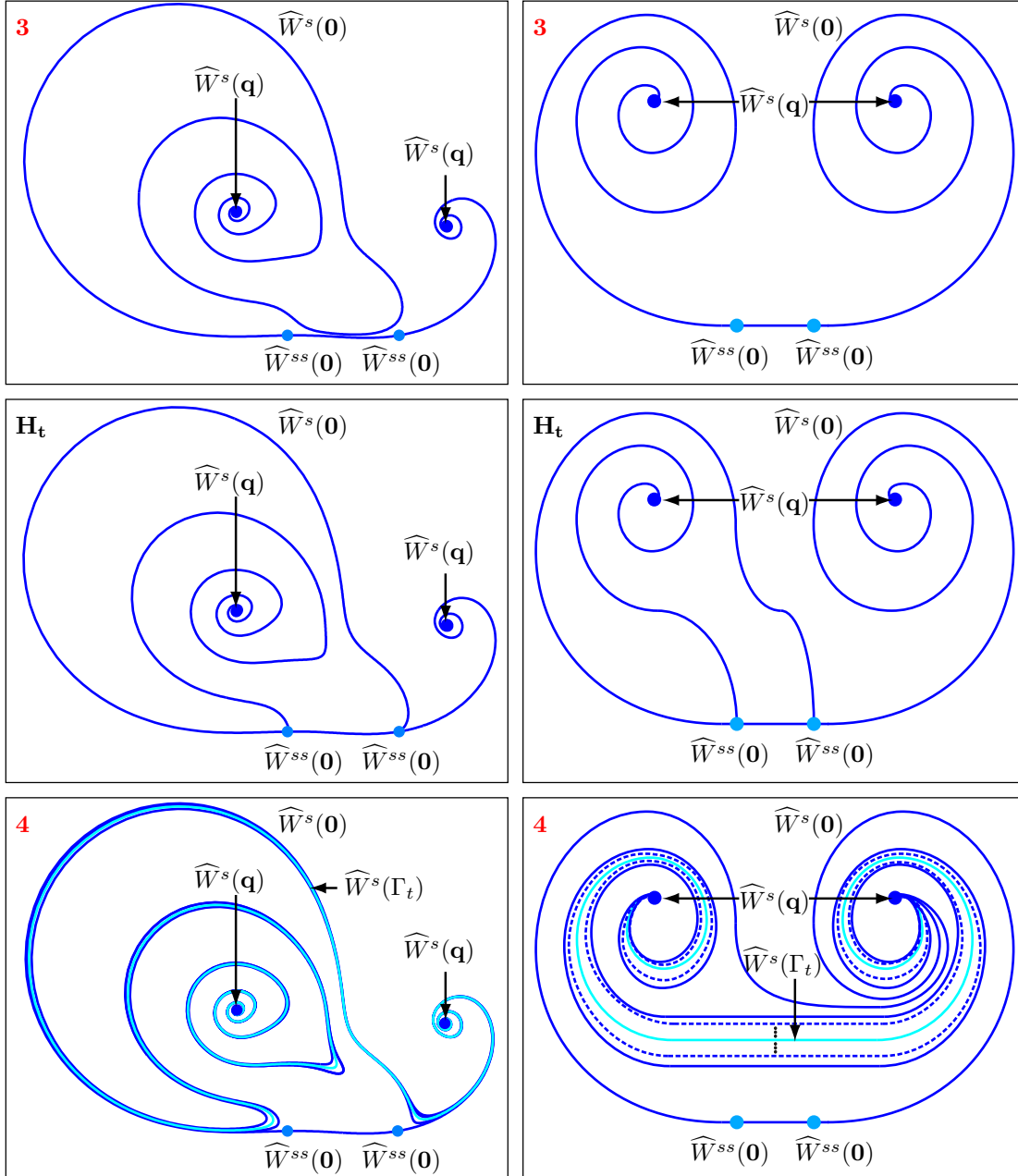


Figure 8: Continued.

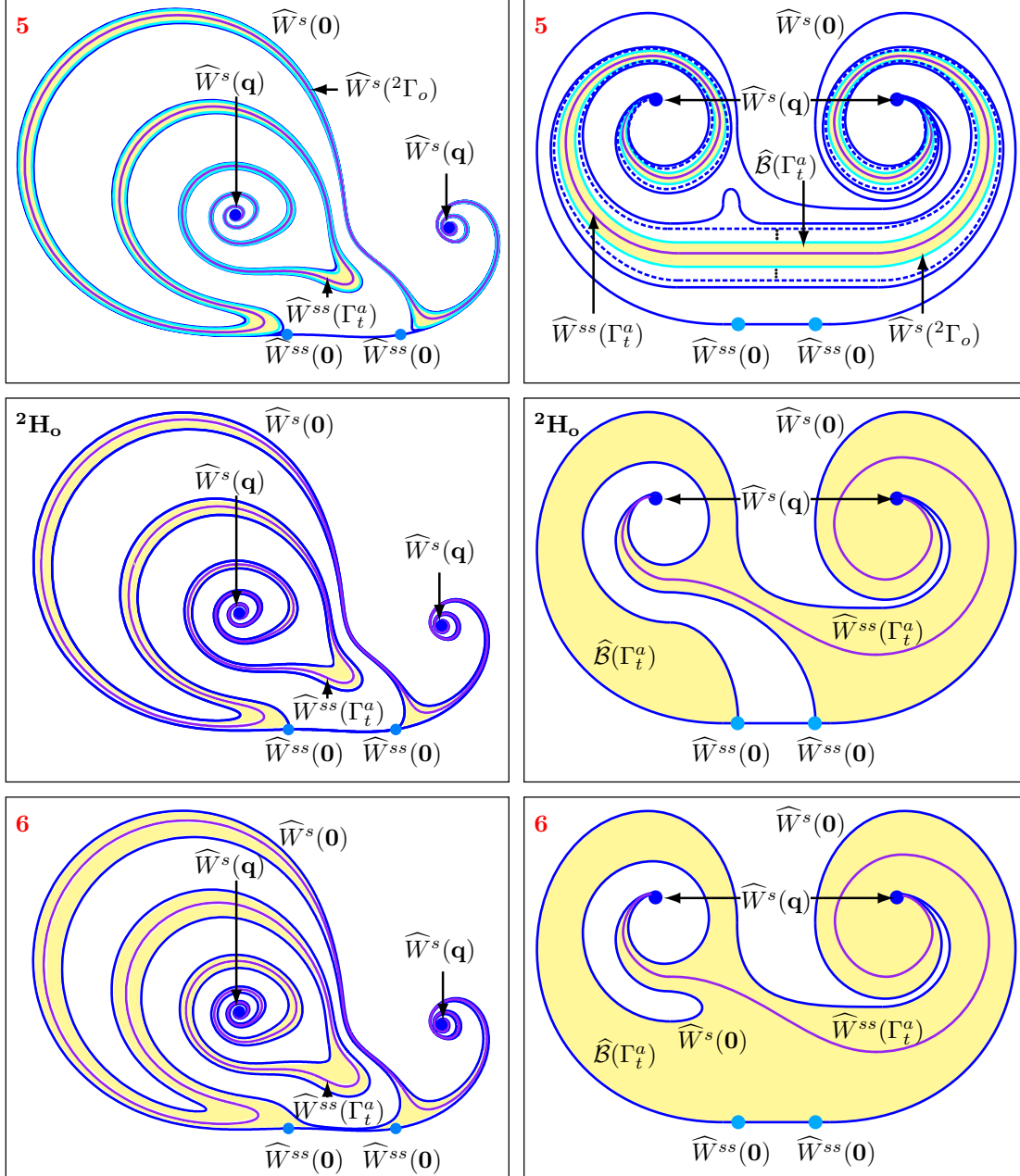


Figure 8: Continued.

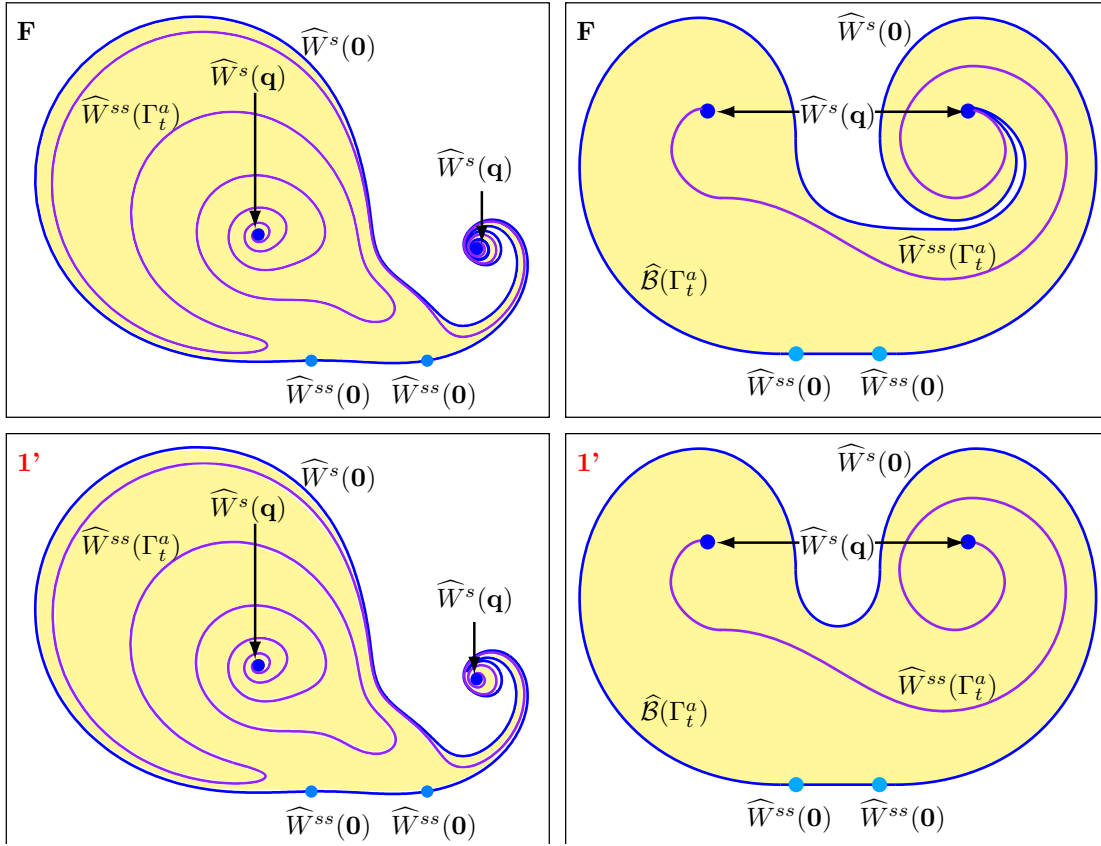


Figure 8: Continued.

set $\widehat{W}^{ss}(\Gamma_o^a)$ (purple curve) of its strong stable manifold intersects \mathbb{S}^* in two closed curves. The boundary of the basin $\mathcal{B}(\Gamma_o^a)$ is formed by $W^s(\mathbf{0})$ and $W^s(\mathbf{q})$; hence, $\partial\widehat{\mathcal{B}}(\Gamma_o^a) = \widehat{W}^s(\mathbf{0}) \cup \widehat{W}^s(\mathbf{q})$. Note that its closure $\widehat{\mathcal{B}}(\Gamma_o^a)$ is topological single closed disk.

Panel **H_o** of fig. 8 shows the homoclinic bifurcation at the boundary between regions **1** and **2**, where $\widehat{W}^s(\mathbf{0})$ closes back on itself along $\widehat{W}^{ss}(\mathbf{0})$. The basin $\widehat{\mathcal{B}}(\Gamma_o^a)$ is now disconnected and $\widehat{\mathcal{B}}(\Gamma_o^a)$ is topologically equivalent to two disjoint disks. Furthermore, not all of $\widehat{W}^s(\mathbf{0})$ is part of $\partial\widehat{\mathcal{B}}(\Gamma_o^a)$ any longer.

In region **2** the homoclinic orbit Γ_{hom} becomes the orientable saddle periodic orbit Γ_o . Instead of $\widehat{W}^s(\mathbf{0})$, the intersection set $\widehat{W}^s(\Gamma_o)$ now forms the outer part of the boundary set of $\widehat{\mathcal{B}}(\Gamma_o^a)$, that is, $\partial\widehat{\mathcal{B}}(\Gamma_o^a) = \widehat{W}^s(\Gamma_o) \cup \widehat{W}^s(\mathbf{q})$. Note that $\widehat{W}^s(\mathbf{0})$ accumulates on $\widehat{W}^s(\Gamma_o)$, which consists of two topological circles, reflecting that $W^s(\Gamma_o)$ is also a cylinder. The accumulation of $\widehat{W}^s(\mathbf{0})$ on $\widehat{W}^s(\Gamma_o)$ is a consequence of the λ -lemma; the structurally stable heteroclinic orbit from Γ_o to $\mathbf{0}$ forces $\widehat{W}^s(\mathbf{0})$ to spiral around $\widehat{W}^s(\Gamma_o)$. We remark that, as the λ -lemma is local in nature, this accumulation may be lost if a bigger sphere is chosen and $\widehat{W}^s(\Gamma_o)$ becomes tangent to the sphere.

The transition from region **2** to region **3** is via a saddle-node bifurcation (**SNP**) of periodic orbits, where Γ_o and Γ_a merge and disappear. As a consequence, $\widehat{W}^s(\Gamma_o)$, $\widehat{W}^{ss}(\Gamma_o^a)$ and $\widehat{\mathcal{B}}(\Gamma_o^a)$ are no longer present in fig. 8 panel **3**. The intersection set $\widehat{W}^s(\mathbf{0})$ now accumulates on $\widehat{W}^s(\mathbf{q})$, which reflects the existence of a structurally stable heteroclinic orbit from \mathbf{q} to $\mathbf{0}$.

3.2.2 Intersection sets in regions 4 and 5

Panel **H_t** of fig. 8 is at the transition between regions **3** and **4**, characterized by a codimension-one non-orientable homoclinic orbit. As for the orientable homoclinic orbit, shown in panel **H_o**, the intersection set $\widehat{W}^s(\mathbf{0})$ connects back on itself at $\widehat{W}^{ss}(\mathbf{0})$, but now $\widehat{W}^s(\mathbf{0})$ does not bound two open regions. Instead, two segments of $\widehat{W}^s(\mathbf{0})$ accumulate on the intersection points $\widehat{W}^s(\mathbf{q})$, due to the persistence of the heteroclinic orbit from \mathbf{q} to $\mathbf{0}$.

In region **4**, the homoclinic orbit Γ_{hom} becomes in the periodic orbit Γ_t . Compare $\widehat{W}^s(\Gamma_o)$ in panel **2** with $\widehat{W}^s(\Gamma_t)$ in panel **4** of fig. 8; for the former, $\widehat{W}^s(\Gamma_o)$ is composed of two closed curves, while for the latter, $W^s(\Gamma_t)$ intersects \mathbb{S}^* in a single curve that accumulates on $\widehat{W}^s(\mathbf{q})$ as a consequence of the existence of a heteroclinic orbit from \mathbf{q} to Γ_t . The intersection set $\widehat{W}^s(\mathbf{0})$ consist of many curve segments; there is a segment that accumulates on a single point in $\widehat{W}^s(\mathbf{q})$, while the other curve segments connect the two intersection points $\widehat{W}^s(\mathbf{q})$. In section 3.1.4, we proved the existence of infinitely many heteroclinic orbits in region **4**; as such, there must be infinitely many curve segments of $\widehat{W}^s(\mathbf{0})$ accumulating on $\widehat{W}^s(\mathbf{q})$. This is a consequence of the λ -lemma when applied to the time-one map of the flow of system (2). Since \mathbb{S}^* is transverse to $W^s(\mathbf{q})$, each transverse heteroclinic orbit from \mathbf{q} to $\mathbf{0}$ creates at least one intersection curve $\widehat{W}^s(\mathbf{0})$ whose endpoints are $\widehat{W}^s(\mathbf{q})$. Furthermore, this set of curves accumulates onto $\widehat{W}^s(\Gamma_t)$. In panel **4** of fig. 8 we only show three of these infinitely many intersection curves of $\widehat{W}^s(\mathbf{0})$; the existence of infinitely many curves is indicated by dashed blue curves; the three dots illustrates their accumulation on $\widehat{W}^s(\Gamma_t)$.

In region **5**, the period-doubling bifurcation **PD** creates ${}^2\Gamma_o$ and Γ_t^a . Note that ${}^2\Gamma_o$ is an orientable periodic orbit, yet its intersection set $\widehat{W}^s({}^2\Gamma_o)$, composed of two open curves, is markedly different from $\widehat{W}^s(\Gamma_o)$ in region **2**. This is due to the existence of the two heteroclinic orbits from \mathbf{q} to ${}^2\Gamma_o$ that force the two curves in $\widehat{W}^s({}^2\Gamma_o)$ to accumulate on $\widehat{W}^s(\mathbf{q})$; see panel **5** of fig. 8. The closure $\widehat{\mathcal{B}}({}^2\Gamma_o^a)$ is a topological circle that bounds $\widehat{\mathcal{B}}(\Gamma_t^a)$, namely, $\partial\widehat{\mathcal{B}}(\Gamma_t^a) = \widehat{W}^s({}^2\Gamma_o) = \widehat{W}^s({}^2\Gamma_o) \cup \widehat{W}^s(\mathbf{q})$. Hence, the manifold $W^s({}^2\Gamma_o)$, together with $W^s(\mathbf{q})$, plays a similar role as $W^s(\Gamma_o)$ in region **2**. The set $\widehat{W}^s(\mathbf{0})$ does not change qualitatively in the transition from region **4** to region **5**, in the sense that all segments are in one-to-one correspondence with their counterparts in region **4**. The only difference is that $\widehat{W}^s(\mathbf{0})$ now accumulates of $\widehat{W}^s({}^2\Gamma_o)$; more precisely, due to the period-doubled nature of ${}^2\Gamma_o$, there are two sets of segments in $\widehat{W}^s(\mathbf{0})$ that accumulate on different curves of $\widehat{W}^s({}^2\Gamma_o)$.

3.2.3 Intersection sets in regions 6 and 1'

Panel ${}^2\mathbf{H}_o$ of fig. 8 shows how the intersection set $\widehat{W}^s(\mathbf{0})$ meets itself transversally at $\widehat{W}^{ss}(\mathbf{0})$ in this bifurcation. As ${}^2\Gamma_o$ becomes ${}^2\Gamma_{\text{hom}}$, the infinitely many curves of $\widehat{W}^s(\mathbf{0})$ in region 4 disappear and only two curves that connect $\widehat{W}^{ss}(\mathbf{0})$ and $\widehat{W}^s(\mathbf{q})$ exist. In addition, $\partial\widehat{\mathcal{B}}(\Gamma_t^a) \subset \widehat{W}^s(\mathbf{0}) \cup \widehat{W}^s(\mathbf{q})$, that is, $W^s(\mathbf{0})$ becomes the new separatrix in phase space. Although \mathbf{H}_o and ${}^2\mathbf{H}_o$ are both codimension-one orientable homoclinic bifurcations, their intersection sets are not homeomorphic, as seen in the respective panels of fig. 8; there exists a non-trivial intersection between $W^u(\mathbf{q})$ and $W^s(\mathbf{0})$ at ${}^2\mathbf{H}_o$.

In region 6, the intersection set $\widehat{W}^s(\mathbf{0})$ bounds $\widehat{\mathcal{B}}(\Gamma_t^a)$, note that $\widehat{\mathcal{B}}(\Gamma_t^a)$ is a topological annulus. The intersection set $\widehat{W}^s(\mathbf{0})$ is composed of two disjoint curves that spiral into the intersection points $\widehat{W}^s(\mathbf{q})$; hence the intersection set $\widehat{\mathcal{B}}(\Gamma_t^a)$ is not a simply connected set, which indicates the persistence of the two heteroclinic orbits from \mathbf{q} to $\mathbf{0}$.

At the fold curve \mathbf{F} , the unstable manifold $W^u(\mathbf{q})$ intersects $W^s(\mathbf{0})$ tangentially in the heteroclinic orbit γ^* ; see panel \mathbf{F} of fig. 5. On the level of the intersection sets in panel \mathbf{F} of fig. 8, the set $\widehat{W}^s(\mathbf{0})$ is formed by one segment that accumulates on both sides on a single point in $\widehat{W}^s(\mathbf{q})$. At this bifurcation, $W^s(\mathbf{0})$ cannot cross $W^u(\mathbf{q})$, as they are in tangency, and $\widehat{\mathcal{B}}(\Gamma_t^a)$ becomes a simply connected set in region 6. Hence, $\widehat{\mathcal{B}}(\Gamma_t^a)$ is homeomorphic to a closed disk, as is the case in region 1.

In region 1', $W^s(\mathbf{0})$ no longer intersects $W^u(\mathbf{q})$ and this is reflected on the level of intersection sets as a disconnection of $\widehat{W}^s(\mathbf{0})$ from both points in $\widehat{W}^s(\mathbf{q})$. Instead $\widehat{W}^s(\mathbf{0})$ encloses $\widehat{W}^s(\mathbf{q})$ and bounds $\widehat{\mathcal{B}}(\Gamma_t^a)$. The only difference with region 1 is the topological difference between $\widehat{W}^{ss}(\Gamma_t^a)$ and $\widehat{W}^{ss}(\Gamma_o^a)$, which are associated with a non-orientable and an orientable attracting periodic orbit, respectively. As the transition through \mathbf{CC}^- involves the disappearance of $\widehat{W}^{ss}(\Gamma_t^a)$, because there is no well-defined strong stable manifold in region 1*, the two topological circles of $\widehat{W}^{ss}(\Gamma_o^a)$ appear only after crossing \mathbf{CC}^+ into region 1. During these transitions, the other intersection curves and basin of attraction do not change qualitatively.

3.3 Transition of the homoclinic orbit through the inclination flip

We now focus specifically on the curve of homoclinic bifurcations and illustrate the transition through the codimension-two homoclinic flip bifurcation point \mathbf{B}_I . As illustrated in, e.g., [31], the two-dimensional manifold $W^s(\mathbf{0})$ can violate genericity condition (G3) in two different ways, which depend on the eigenvalues of the equilibrium; namely, whether $|\lambda^{ss}| > 2|\lambda^s|$ is fulfilled or not. Despite this difference, both mechanisms unfold in the same way. Condition $|\lambda^{ss}| < 2|\lambda^s|$ was considered in [1] in the transition through the inclination flip point \mathbf{A}_I of case A. Here, we illustrate the transition through the inclination flip point \mathbf{B}_I of case B for the case that $|\lambda^{ss}| > 2|\lambda^s|$.

fig. 9 shows the transition through \mathbf{B}_I on the level of the invariant manifolds in the left column, and their respective intersection sets with \mathbb{S}^* in the right column. We show again the stereographic projections of the intersection sets at \mathbf{H}_o and \mathbf{H}_t for comparison purposes. In the accompanying animation ([GKO_Bflip_animatedFig9.gif](#)) the phase portraits of fig. 9 are rotated clockwise around the y -axis. At the codimension-one orientable homoclinic bifurcation in panel \mathbf{H}_o , the branch of $W^u(\mathbf{0})$ that spirals towards Γ_o^a in region 1 now forms the homoclinic orbit Γ_{hom} , while the manifold $W^u(\mathbf{q})$ accumulates onto Γ_o^a . Note that Γ_{hom} returns to $\mathbf{0}$ along a direction that is clearly transverse to $W^{ss}(\mathbf{0})$ (light-blue curve) and $W^s(\mathbf{0})$ closes back on itself along $W^{ss}(\mathbf{0})$. Furthermore, $W^s(\mathbf{0})$ is topologically a cylinder; compare with fig. 1(a1). On the level of intersection sets, $\widehat{W}^s(\mathbf{0})$ closes on $\widehat{W}^{ss}(\mathbf{0})$, so that the basin of attraction $\widehat{\mathcal{B}}(\Gamma_o^a)$ is a disconnected set. At the codimension-two point \mathbf{B}_I , the middle of fig. 9, the surface $W^s(\mathbf{0})$ closes back on itself at $W^{ss}(\mathbf{0})$ in such a way that it makes a quadratic tangency with itself at $W^{ss}(\mathbf{0})$; the bottom panel of Fig. 2. in [31] is misleading in this respect. Hence, if we follow the tangent plane of $W^s(\mathbf{0})$ along Γ_{hom} as $t \rightarrow -\infty$, it does not contain the strong stable eigenvector of $\mathbf{0}$; this violates genericity condition (G3). As a result, $W^s(\mathbf{0})$ meets and closes along a single branch of $W^{ss}(\mathbf{0})$. Additionally, the attracting periodic orbit Γ_o^a is now the homoclinic orbit Γ_{hom} , making it the boundary of $W^u(\mathbf{q})$ in phase space. On the level of intersection sets, both parts of $\widehat{W}^s(\mathbf{0})$ have a tangency with itself at only one of the intersection points of $\widehat{W}^{ss}(\mathbf{0})$. Finally, at the codimension-one non-orientable homoclinic bifurcation in panel \mathbf{H}_t , the stable manifold $W^s(\mathbf{0})$ makes half a twist before closing along (both branches) of $W^{ss}(\mathbf{0})$, so that the homoclinic orbit is non-orientable. An interesting difference between \mathbf{H}_o and \mathbf{H}_t is the existence of the heteroclinic orbit γ_1 in panel \mathbf{H}_t , caused

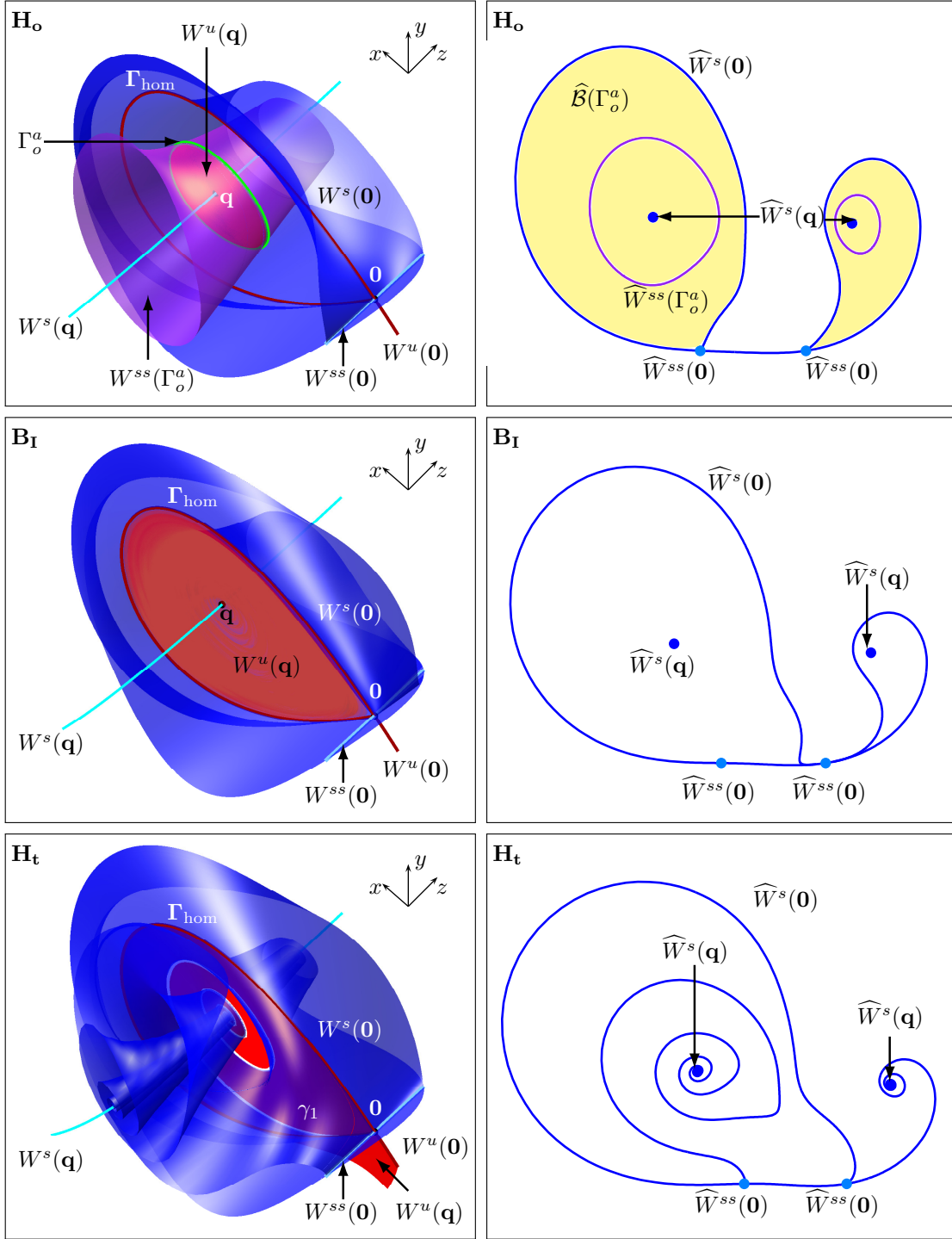


Figure 9: Transition along the homoclinic bifurcation through the inclination flip bifurcation B_I of system (2). Shown are different manifolds in \mathbb{R}^3 (left column) and their respective stereographic projections (right column). The color code is in fig. 6 and the parameter values are given in table 2. See also the accompanying animation ([GKO_Bflip_animatedFig9.gif](#)).

Homoclinic	\mathbf{H}_o	\mathbf{B}_o	\mathbf{H}_t	${}^2\mathbf{H}_o$	\mathbf{F}
μ	-0.150000000	0.0	0.150000000	0.150000000	0.150000000
$\tilde{\mu}$	-0.062331201	0.0	0.062381076	0.069351963	0.070562587

Table 3: Chosen representative parameter values at selected bifurcations in fig. 11.

Region	1	2	3	4	5	6
μ	-0.150	-0.150	0.150	0.150	0.150	0.150
$\tilde{\mu}$	-0.060	-0.065	0.060	0.065	0.069	0.070

Table 4: Chosen representative parameter values for the different open regions in fig. 11.

by the transverse intersection of $W^s(\mathbf{0})$ and $W^u(\mathbf{q})$. In fact, the long excursion of γ_1 around \mathbf{q} becomes Γ_{hom} at \mathbf{B}_t . On the level of the intersection sets, $\widehat{W}^s(\mathbf{0})$ consists of two curves that accumulates on $\widehat{W}^s(\mathbf{q})$, as a consequence of the existence of γ_1 .

By looking at the stereographic projection in the right column of fig. 9, we can see a clearer difference between the two conditions. Condition $|\lambda^{ss}| < 2|\lambda^s|$, as considered in [1] for the case **A**, leads to a limit at the moment of the inclination flip, where one end of the intersection set $\widehat{W}^s(\mathbf{0})$ spirals into one of the points in $\widehat{W}^s(\mathbf{q})$; this is similar to the right segment in \mathbf{H}_t ; the other end closes back on $\widehat{W}^s(\mathbf{0})$, but along the weak direction of $W^s(\mathbf{0})$; see Fig. 13 of [1]. In contrast, condition $|\lambda^{ss}| > 2|\lambda^s|$ as considered here for case **B**, leads to a limit at the moment of the inclination flip, at which the intersection set $\widehat{W}^s(\mathbf{0})$ closes tangentially at only one of the intersection points of $\widehat{W}^{ss}(\mathbf{0})$.

4 Orbit flip of case B

A codimension-two orbit flip bifurcation occurs when condition **(G2)** is violated, that is, the homoclinic orbit Γ_{hom} is a subset of the strong stable manifold $W^{ss}(\mathbf{0})$. Even though the mechanism is different from that of the inclination flip, the orbit flip also results in a change from an orientable to a non-orientable codimension-one homoclinic bifurcation; moreover, the theoretical unfoldings of both codimension-two points are the same [38]. We now demonstrate that both bifurcations also have the same topological organization on the level of the manifolds involved. Here, we consider case **B**, meaning that, the equilibrium $\mathbf{0}$ satisfies the eigenvalue conditions as given in section 2.1.

We start by the transition of the homoclinic orbit through the orbit flip bifurcation \mathbf{B}_o . fig. 10 shows the phase portraits and the intersection sets with \mathbb{S}^* at the bifurcations \mathbf{H}_o , \mathbf{B}_o and \mathbf{H}_t at the parameter values given as in table 3. Note that the panels \mathbf{H}_o and \mathbf{H}_t are topologically equivalent to the respective panels in fig. 9 for the inclination flip, but panel \mathbf{B}_o is different. At the moment of the orbit flip, the one-dimensional strong stable manifold $W^{ss}(\mathbf{0})$ intersects \mathbb{S}^* in a single point, because the other branch of $W^{ss}(\mathbf{0})$ is Γ_{hom} . Hence, only one end of $\widehat{W}^s(\mathbf{0})$ closes back on itself. The other end spirals into one point of $\widehat{W}^s(\mathbf{q})$, but at an algebraic rather than an exponential rate; we indicate this accumulation by a light-blue shading. Note that the relative position of the points in $\widehat{W}^{ss}(\mathbf{0})$ swaps before and after the orbit flip; see panels \mathbf{H}_o and \mathbf{H}_t in fig. 10. Unlike the case **IF**, the case **OF** does not have multiple ways of breaking condition **(G2)** that depends on additional eigenvalue conditions. Furthermore, the results that we find for the transition for the orbit flip of type **B** are topologically equivalent to those found for case **A** [1].

We now present the unfolding of the orbit flip bifurcation \mathbf{B}_o with respect to the parameters μ and $\tilde{\mu}$. fig. 11 shows the bifurcation diagram locally near the codimension-two orbit flip point \mathbf{B}_o in the $(\mu, \tilde{\mu})$ -plane; here we use the coordinate transformation $\hat{\mu} := 10(\tilde{\mu} - 0.4157\mu)$ to improve the visualization. Close to \mathbf{B}_o , the bifurcation diagram is topologically equivalent to the bifurcation diagram of the inclination flip; see fig. 5. In particular, we also find the fold **F** of heteroclinic orbits, and the curves \mathbf{CC}^+ and \mathbf{CC}^- in the same relative positions with respect to the other bifurcation curves. As we did for the inclination flip in section 3, we use the bifurcation diagram in fig. 11 as a reference to describe the re-organization of the global manifolds in

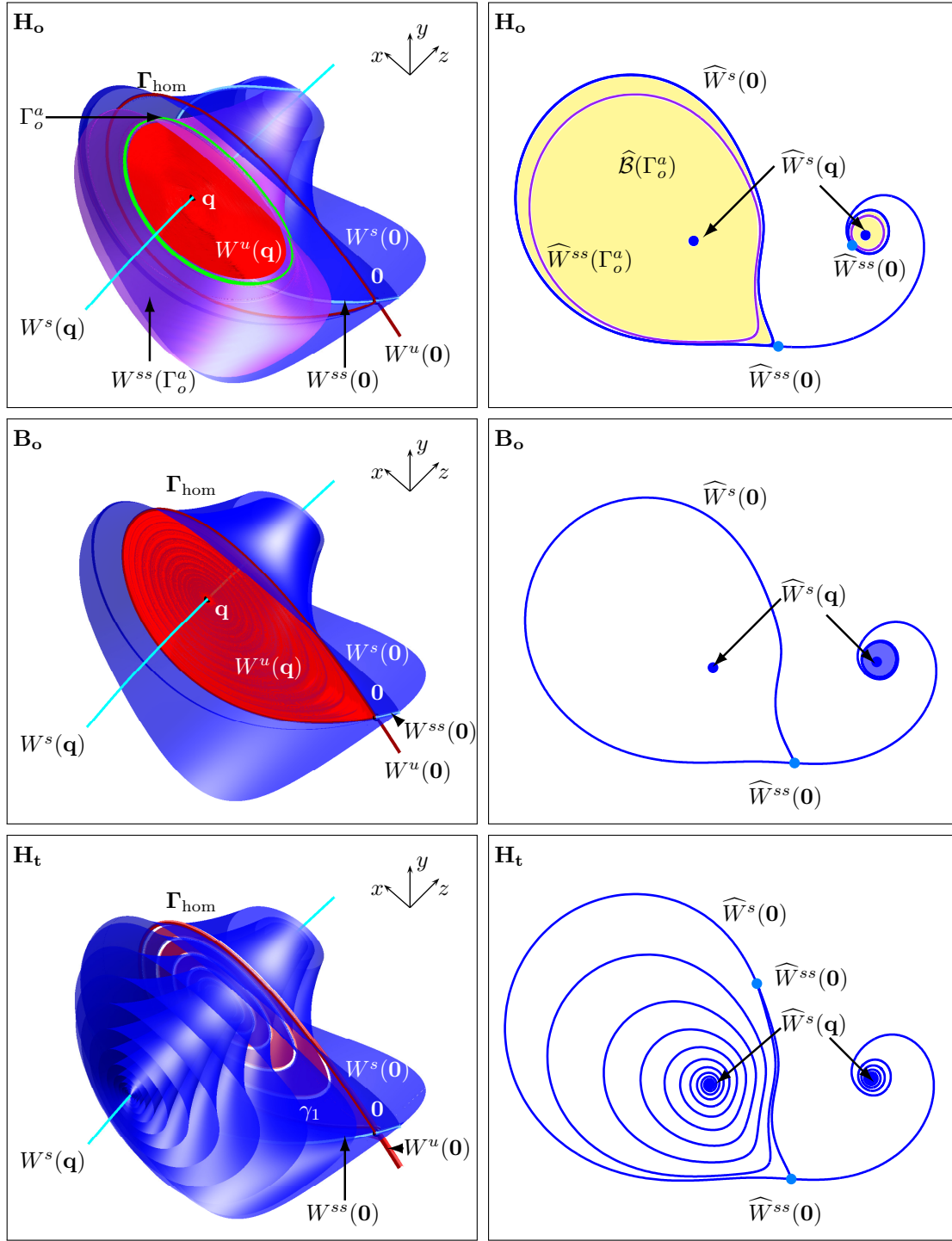


Figure 10: Transition along the homoclinic bifurcation through the orbit flip bifurcation \mathbf{B}_o of system (2). Shown are different manifolds in \mathbb{R}^3 (left column) and their respective stereographic projections (right column). The color code is in fig. 6 and the parameter values are given in table 3.

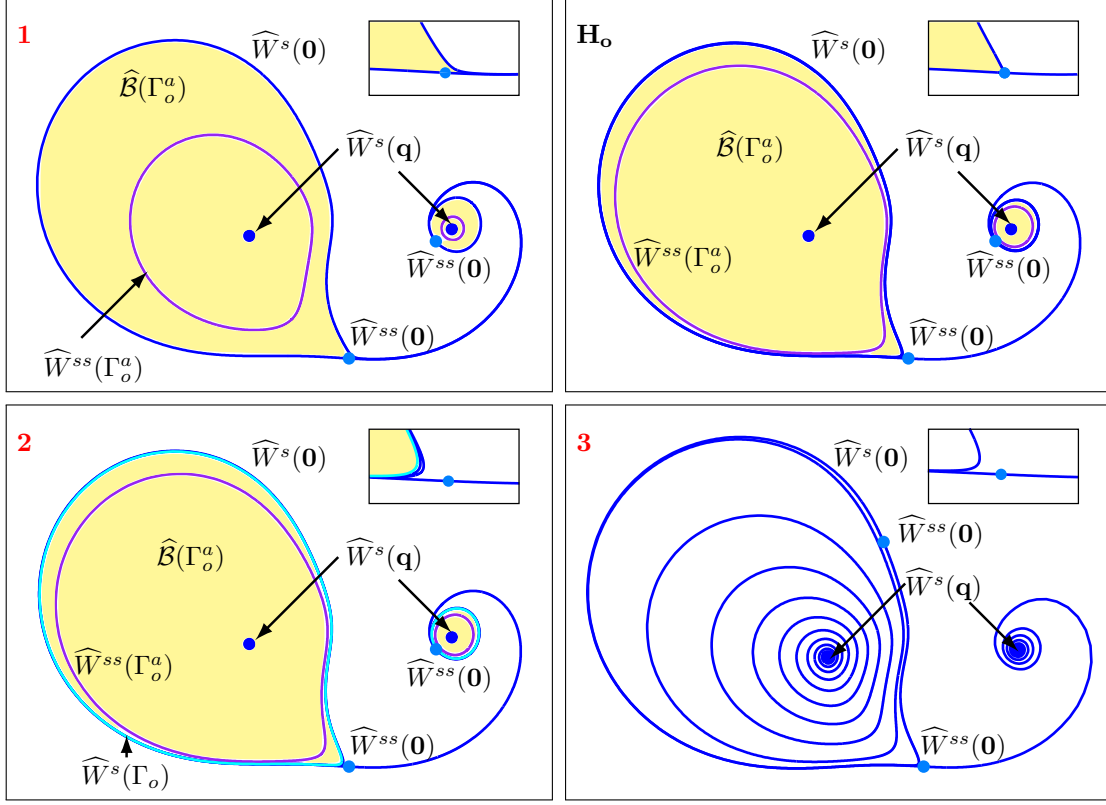


Figure 12: Stereographic projections of the intersection sets of the invariant manifolds with \mathbb{S}^* in the regions and at bifurcations of the bifurcation diagram in fig. 11 near the orbit flip \mathbf{B}_o . The insets show enlargements around one of the points of $\widehat{W}^{ss}(\mathbf{0})$. The color code and nomenclature of the regions is the same as given in fig. 5 and fig. 8. For respective parameter values see table 4 and table 3.

Our approach was to compute $W^s(\mathbf{0})$ as a global object in phase space to study how it re-arranges itself as the system undergoes different bifurcations. Moreover, we determined the two-dimensional stable and unstable manifolds of the saddle periodic orbits that co-exist in certain regions of parameters space and studied their interaction with $W^s(\mathbf{0})$. We also computed the intersection sets of the stable manifolds with a suitable sphere \mathbb{S}^* , chosen such that it contains all compact invariant objects close to $\mathbf{0}$. In particular, knowledge of the intersection sets on \mathbb{S}^* allowed us to clarify the properties of basins of attraction. Our numerical results confirm that the local two-parameter unfoldings of both inclination and orbit flip bifurcations of case **B** are the same, even on the level of the interacting global manifolds including those of \mathbf{q} ; the only difference lies in the phase portraits at the codimension-two points \mathbf{B}_o and \mathbf{B}_I .

Our findings can be summarized as follows:

Results (manifold structure near flip bifurcation of case **B**). *Consider system (2) near an inclination flip or an orbit flip homoclinic bifurcation of case **B** at the origin, such that there also exists a nearby unstable saddle-focus \mathbf{q} . For an inclination and orbit flip the bifurcation diagram is topologically equivalent to the ones shown in fig. 5 and fig. 11; where regions and bifurcations are labelled according to section 3. The configurations of the manifolds in phase space and their intersection sets with \mathbb{S}^* are as follows,*

B_I *At the codimension-two inclination flip point \mathbf{B}_I , the intersection set $\widehat{W}^s(\mathbf{0})$ on \mathbb{S}^* is a closed curve tangent to itself at one of the two points in $\widehat{W}^{ss}(\mathbf{0})$. The stable manifold $W^s(\mathbf{0})$ in \mathbb{R}^3 closes back on itself along a single branch of $W^{ss}(\mathbf{0})$. More precisely, we find that $W^s(\mathbf{0})$ has a quadratic tangency with itself at $W^{ss}(\mathbf{0})$. The unstable manifold $W^u(\mathbf{q})$ accumulates on Γ_{hom} .*

B_o *At the codimension-two orbit flip point \mathbf{B}_o , the intersection set $\widehat{W}^s(\mathbf{0})$ closes on itself at only one point of $\widehat{W}^{ss}(\mathbf{0})$, because the second intersection point $\widehat{W}^{ss}(\mathbf{0})$ becomes the homoclinic orbit and does not*

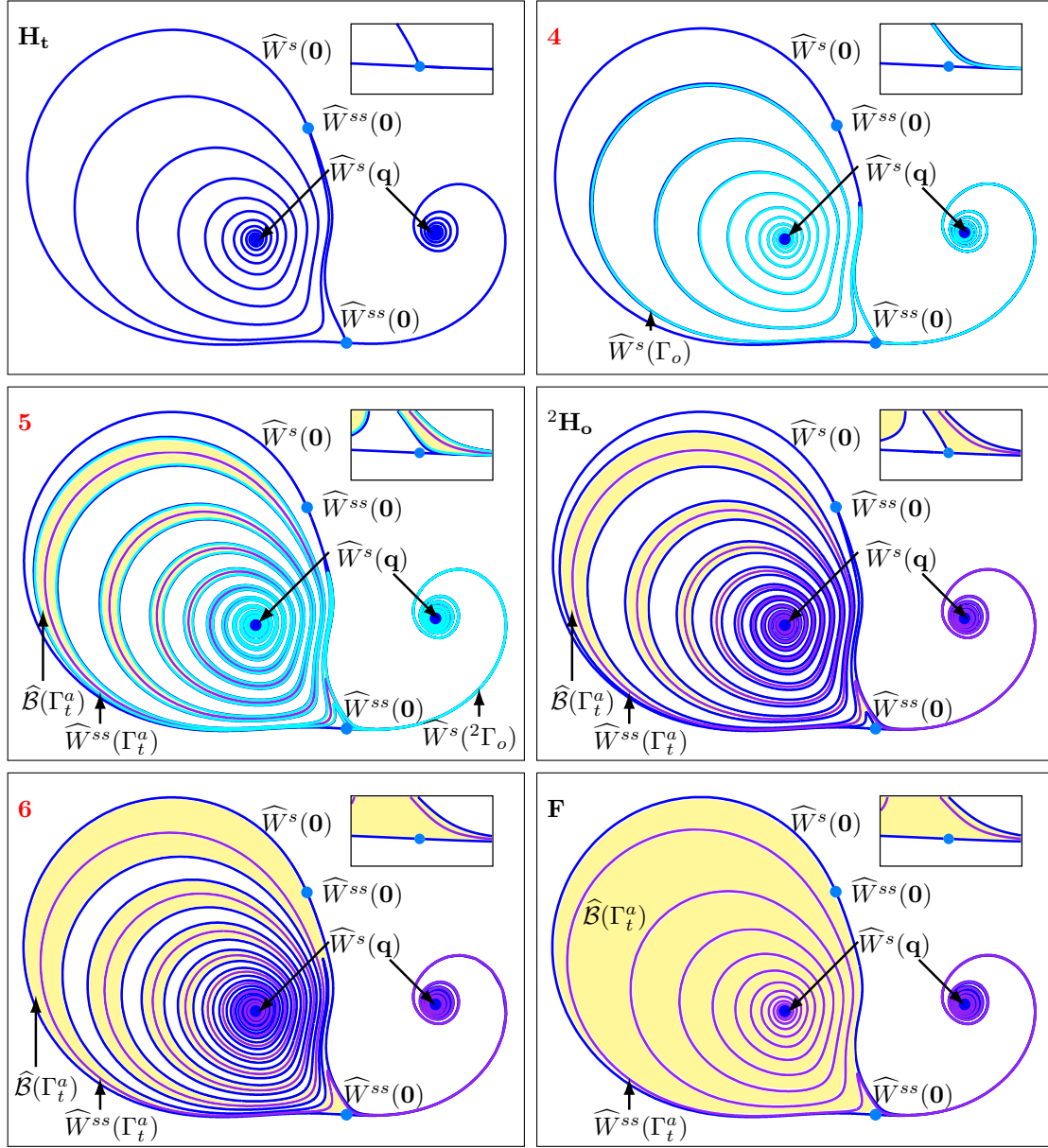


Figure 12: Continued.

intersect \mathbb{S}^* . The segment $\widehat{W}^s(\mathbf{0})$ on the other side of $\widehat{W}^{ss}(\mathbf{0})$ accumulates on $\widehat{W}^s(\mathbf{q})$. The homoclinic orbit bounds the two-dimensional manifold $W^u(\mathbf{q})$ and part of $W^s(\mathbf{0})$ accumulates on $W^s(\mathbf{q})$.

1 In region **1** the intersection set $\widehat{W}^s(\mathbf{0})$ of the stable manifold of $\mathbf{0}$ encloses the basin of attraction $\widehat{\mathcal{B}}(\Gamma_o^a)$ of the orientable attracting periodic orbit Γ_o^a ; here, $\widehat{\mathcal{B}}(\Gamma_o^a)$ is a connected set and its closure is homeomorphic to a disk, and $\widehat{W}^{ss}(\Gamma_o^a)$ is the union of two topological circles. The stable manifold $W^s(\mathbf{0})$ is the boundary of the basin of attraction of Γ_o^a , and the unstable manifold $W^u(\mathbf{q})$ is bounded by the attracting periodic orbit Γ_o^a .

H_o Along the orientable homoclinic curve **H_o**, the intersection set $\widehat{W}^s(\mathbf{0})$ closes on itself at $\widehat{W}^{ss}(\mathbf{0})$ and encloses the region $\widehat{\mathcal{B}}(\Gamma_o^a)$. The closure of $\widehat{\mathcal{B}}(\Gamma_o^a)$ is now homeomorphic to two disks. The stable manifold $W^s(\mathbf{0})$ closes along $W^{ss}(\mathbf{0})$ and creates a homoclinic orbit Γ_{hom} that forms the boundary of $W^u(\mathbf{q})$.

2 In region **2** there exists a saddle periodic orbit Γ_o . The intersection set $\widehat{W}^s(\mathbf{0})$ spirals towards $\widehat{W}^s(\Gamma_o)$. The closure of $\widehat{\mathcal{B}}(\Gamma_o^a)$ is homeomorphic to two disk that are each bounded by a topological circle in $\widehat{W}^s(\Gamma_o)$. The stable manifold $W^s(\Gamma_o)$ is the boundary of $\mathcal{B}(\Gamma_o^a)$, and $W^u(\mathbf{q})$ is contained in $\mathcal{B}(\Gamma_o^a)$ and accumulates on Γ_o . Furthermore, $W^u(\Gamma_o)$ intersects $W^s(\mathbf{0})$ in a structurally stable heteroclinic orbit.

SNP At the curve of saddle-node of periodic orbit **SNP**, the periodic orbits Γ_o^a and Γ_o merge into a non-hyperbolic periodic orbit and disappear in region **3**.

3 In region **3**, the segment of the intersection set $\widehat{W}^s(\mathbf{0})$ spirals towards $\widehat{W}^s(\mathbf{q})$. There exists a structurally stable heteroclinic orbit γ_1 from \mathbf{q} to $\mathbf{0}$, and $W^u(\mathbf{q})$ is bounded by the unstable manifold $W^u(\mathbf{0})$.

H_t Along the non-orientable homoclinic curve **H_t**, the homoclinic orbit Γ_{hom} exists, the intersection set $\widehat{W}^s(\mathbf{0})$ closes on itself at $\widehat{W}^{ss}(\mathbf{0})$, and segments of it accumulate on $\widehat{W}^s(\mathbf{q})$. The stable manifold $W^s(\mathbf{0})$ closes along $W^{ss}(\mathbf{0})$, while it intersects $W^u(\mathbf{q})$ transversally.

4 In region **4** there exists the periodic orbit Γ_t . The intersection set $\widehat{W}^s(\mathbf{0})$ consists of infinitely many curves that spiral towards $\widehat{W}^s(\mathbf{q})$ and accumulate on $\widehat{W}^s(\Gamma_t)$, which also spirals towards $\widehat{W}^s(\mathbf{q})$. There exists one structurally stable heteroclinic orbit from Γ_t to $\mathbf{0}$ and one from \mathbf{q} to Γ_t . Furthermore, there are infinitely many structurally stable heteroclinic orbits from \mathbf{q} to $\mathbf{0}$. The unstable manifold $W^u(\mathbf{0})$ bounds both $W^u(\Gamma_t)$ and $W^u(\mathbf{q})$.

PD Along the period-doubling bifurcation curve **PD**, the periodic orbit Γ_t is non-hyperbolic. It turns into an attracting periodic orbit Γ_t^a and creates the period-doubled periodic orbit ${}^2\Gamma_o$ in region **5**.

5 In region **5**, the intersection set $\widehat{W}^s({}^2\Gamma_o)$ consists of two curves that spiral towards $\widehat{W}^s(\mathbf{q})$ and enclose $\widehat{\mathcal{B}}(\Gamma_t^a)$. In a neighborhood of these curves, there are infinitely many curves $\widehat{W}^s(\mathbf{0})$ that spiral towards $\widehat{W}^s(\mathbf{q})$. Furthermore, $\widehat{W}^{ss}(\Gamma_t^a)$ also spirals towards $\widehat{W}^s(\mathbf{q})$. The stable manifold $W^s({}^2\Gamma_o)$ is the boundary of the basin of attraction of Γ_t^a . There exist a structurally stable heteroclinic orbit from ${}^2\Gamma_o$ to $\mathbf{0}$ and two from \mathbf{q} to ${}^2\Gamma_o$. Also, there are infinitely many structurally stable heteroclinic orbits from \mathbf{q} to $\mathbf{0}$. Moreover, the part of $W^u(\mathbf{q})$ bounded by the two heteroclinic orbits from \mathbf{q} to ${}^2\Gamma_o$ accumulates on Γ_t^a , while the other part is bounded by $W^u(\mathbf{0})$.

²H_o Along the curve **²H_o** the periodic orbit ${}^2\Gamma_o$ disappears and the homoclinic orbit ${}^2\Gamma_{\text{hom}}$ is created. The intersection set $\widehat{W}^s(\mathbf{0})$ consists of curves that close along $\widehat{W}^{ss}(\mathbf{0})$ or spiral towards $\widehat{W}^s(\mathbf{q})$. In the process, $\widehat{W}^s(\mathbf{0})$ encloses $\widehat{\mathcal{B}}(\Gamma_t^a)$. The stable manifold $W^s(\mathbf{0})$ is the boundary of $\mathcal{B}(\Gamma_t^a)$. Furthermore, infinitely many heteroclinic orbits from \mathbf{q} to $\mathbf{0}$ disappear at once, and only two are preserved.

6 In region **6** the intersection set $\widehat{W}^s(\mathbf{0})$ forms the boundary of $\widehat{\mathcal{B}}(\Gamma_t^a)$ and the closure of their union is homeomorphic to an annulus.

F Along the fold **F** of heteroclinic orbits, the intersection set $\widehat{W}^s(\mathbf{0})$ encloses $\widehat{\mathcal{B}}(\Gamma_t^a)$ but only one curve of $\widehat{W}^s(\mathbf{0})$ goes to $\widehat{W}^s(\mathbf{q})$. Moreover, the closure of $\widehat{\mathcal{B}}(\Gamma_o^a)$ is again a topological disk. The stable manifold $W^s(\mathbf{0})$ is tangent to $W^u(\mathbf{q})$ at the heteroclinic orbit γ^* ; this tangency is quadratic.

- 1'** In region **1'**, the intersection set $\widehat{W}^s(\mathbf{0})$ no longer accumulates on $\widehat{W}^s(\mathbf{q})$; the situation is topologically equivalent to that in region **1** except that $\widehat{W}^{ss}(\Gamma_t^a)$ accumulates on $\widehat{W}^s(\mathbf{q})$. In phase space, $W^u(\mathbf{q})$ accumulates on Γ_t^a , and the heteroclinic orbits between \mathbf{q} and $\mathbf{0}$ have disappeared.
- CC⁻** At the curve **CC⁻**, the nontrivial Floquet multipliers of Γ^a are both the same negative real number, meaning that the periodic orbit Γ_t^a becomes Γ^a . There does not exist a well-defined strong stable manifold $W^{ss}(\Gamma^a)$.
- 1*** in region **1*** the Floquet multipliers of Γ^a are complex conjugate and their real part becomes positive when approaching the curve **CC⁺**
- CC⁺** At the curve **CC⁺**, the nontrivial Floquet multipliers of Γ^a are both the same positive number. In the transition to region **1**, the periodic orbit Γ^a becomes Γ_o^a and there exists a well-defined strong stable manifold $W^{ss}(\Gamma_o^a)$.

As discussed before, the existence of \mathbf{q} induces new phenomena in the unfolding of an homoclinic flip bifurcation, even though it does not lie in a tubular neighbourhood of the homoclinic orbit. It is worth noting that we found parameter regimes of system (2) with none or several additional equilibria. Of particular interest is the situation where no additional equilibria exist; since $W^s(\mathbf{q})$ plays an important role in the overall organization of the two-dimensional global manifolds, we conjecture that a one-dimensional manifold from infinity then takes on the role of $W^s(\mathbf{q})$. The compactified version of system (2) should help with answering this question.

In ongoing work we intend to understand the nature of the global manifolds close to the most challenging case of a homoclinic flip bifurcation of case **C**. Its unfolding features infinitely many codimension-one homoclinic bifurcations and period-doubling cascades; this creates horseshoe-regions in the parameter plane that are bounded by tangencies of different manifolds.

A Poincaré Compactification

To describe Poincaré compactification [8, 12] of the three-dimensional vector field (2). We first describe the Poincaré compactification for a one-dimensional system on \mathbb{R} . As is illustrated in fig. 13(a), the one-dimensional phase space (purple curve) is identified with the tangent space of the one-dimensional sphere, the circle $\mathbb{S} \subset \mathbb{R}^2$, at its north pole $(0, 1) \in \mathbb{R}^2$. Each point $r \in \mathbb{R}$ (green dot) is related via inverse central projections f_{\pm} to antipodal points $f_{\pm}(r) \in \mathbb{S}$, one on the upper half sphere \mathbb{S}_+ (red dot) and one on the lower half sphere \mathbb{S}_- (blue dot). In a second step, shown in fig. 13(b), The south-pole projection g is used to map the northern hemisphere \mathbb{S}_+ to the interval $(-2, 2)$ and the equator \mathbb{S}^0 to its boundary $\{-2, 2\}$. Note that g maps $\mathbb{S}_- \setminus \{(0, -1)\}$ to the two open intervals $(-\infty, -2)$ and $(2, \infty)$, which constitutes a second transformation of \mathbb{R} that is not compact. For our purposes, it makes sense to work with \mathbb{S}_+ only.

To understand how a vector field X defined in \mathbb{R} is transformed by the maps f_{\pm} we refer to the following commutative diagram:

$$\begin{array}{ccc} \mathbb{R} & \xrightarrow{f_{\pm}} & \mathbb{S}_{\pm} \\ X \downarrow & & \downarrow X_{\mathbb{S}_{\pm}} \\ \mathrm{TR} = \mathbb{R} & \xrightarrow{Df_{\pm}} & \mathrm{TS}_{\pm} \end{array}$$

Here, TR and TS_{\pm} are the respective tangent bundles of \mathbb{R} and \mathbb{S}_{\pm} , the map Df_{\pm} is the Jacobian of f_{\pm} , and the two vector fields $X_{\mathbb{S}_+}$ and $X_{\mathbb{S}_-}$ defined on \mathbb{S}_+ and \mathbb{S}_- are conjugate to X , respectively. Consequently, we can write the transformed vector field $X_{\mathbb{S}_{\pm}}$ as $X_{\mathbb{S}_{\pm}} = Df_{\pm} \circ X \circ f_{\pm}^{-1}$. It is possible to extend the domain of definition of $X_{\mathbb{S}_{\pm}}$ to the whole of \mathbb{S} provided X is polynomial; when doing this, the dynamics at the equator of \mathbb{S} are invariant and represent the dynamics at infinity of X . Let $\rho(X)$ be the extension of $X_{\mathbb{S}_{\pm}}$ in \mathbb{S} . We have that g generates the vector field $\overline{X} = Dg \circ \rho(X) \circ g^{-1}$ on \mathbb{R} , where the flow on $(-2, 2)$ is conjugate to the flow of X and $\{-2, 2\}$ represents the dynamics at infinity. This procedure can be generalized to higher dimensions, the best-known case is the compactification to the Poincaré-disk of polynomial vector fields on \mathbb{R}^2 [8, 12]. We are interested here in \mathbb{R}^3 , which has been studied for certain models [25, 26, 27, 44] through the use of coordinate charts.

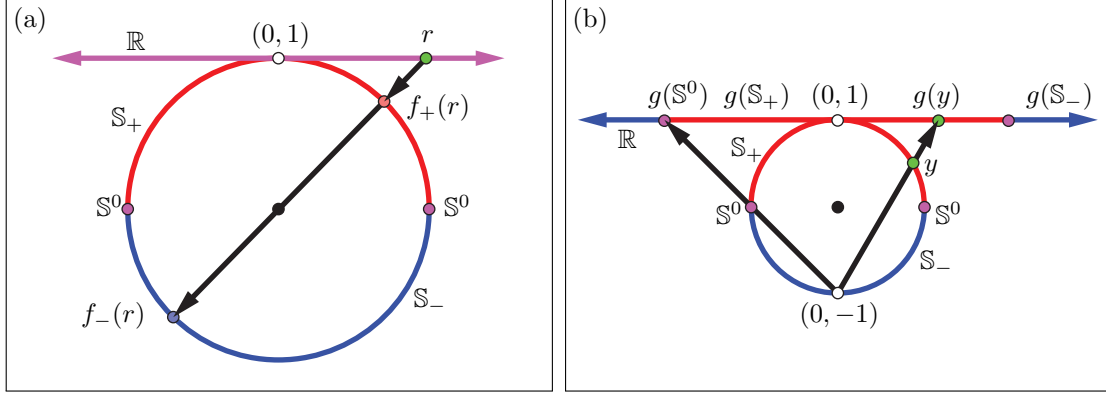


Figure 13: Sketches of the transformations for Poincaré compactification of \mathbb{R} . Panel (a) shows how the central projection sends \mathbb{R} (purple curve) to the upper (red) and the lower (blue) hemispheres of the circle, denoted \mathbb{S}_+ and \mathbb{S}_- , respectively. In panel (b), the stereographic projection from the south pole is applied to send \mathbb{S}_\pm back to the intervals on the real line, as indicated by the corresponding colors.

A.1 Compactification of \mathbb{R}^3

Recall that system (2) is defined as the polynomial vector field

$$X^s(x, y, z) : \begin{cases} \dot{x} = P^1(x, y, z) := ax + by - ax^2 + (\tilde{\mu} - \alpha z)x(2 - 3x), \\ \dot{y} = P^2(x, y, z) := bx + ay - \frac{3}{2}bx^2 - \frac{3}{2}axy - 2y(\tilde{\mu} - \alpha z), \\ \dot{z} = P^3(x, y, z) := cz + \mu x + \gamma xz + \alpha\beta(x^2(1 - x) - y^2), \end{cases}$$

for $(x, y, z) \in \mathbb{R}^3$. We wish to apply a conjugacy transformation such that X^s is topologically equivalent to a vector field \bar{X} when restricted to the open ball $\mathbb{B}^2(2) \subset \mathbb{R}^3$ of radius 2. As the first step, we extend the system into \mathbb{R}^4 , that is, we transform system (2) such that it is defined on the unit hypersphere \mathbb{S}^3 . Then the two-dimensional sphere

$$\mathbb{S}_{\mathbb{R}^4}^2 := \{(x_1, x_2, x_3, x_4) \in \mathbb{S}^3 : x_4 = 0\} \subset \mathbb{R}^4$$

is the equator that contains the dynamics at infinity of system (2). Analogous to the one-dimensional case, we use the inverse central projections $f_\pm : \mathbb{R}^3 \rightarrow \mathbb{S}_\pm^3$ defined by $f_\pm(x_1, x_2, x_3) = \pm(x_1, x_2, x_3, 1)/(1 + x_1^2 + x_2^2 + x_3^2)^{1/2}$; note that the radius $x_1^2 + x_2^2 + x_3^2$ plays the exact same role as r^2 in the one-dimensional example. We perform a conjugacy transformation to the vector field X^s on \mathbb{R}^3 so that we obtain the vector fields $X_{\mathbb{S}_\pm}^s = Df_\pm \circ X^s \circ f_\pm^{-1}$ defined on the tangent bundle $T\mathbb{S}_\pm^3$. It turns out that both X_+^s and X_-^s can be expressed as

$$X_{\mathbb{S}_\pm}^s(y) = y_4 \begin{pmatrix} 1 - y_1^2 & -y_1y_2 & -y_1y_3 \\ -y_1y_2 & 1 - y_2^2 & -y_2y_3 \\ -y_1y_3 & -y_2y_3 & 1 - y_3^2 \\ -y_1y_4 & -y_2y_4 & -y_3y_4 \end{pmatrix} \circ X^s\left(\frac{y_1}{y_4}, \frac{y_2}{y_4}, \frac{y_3}{y_4}\right), \quad (5)$$

where $y = (y_1, y_2, y_3, y_4) \in \mathbb{S}_\pm^3$.

System (5) is not well defined on the hyperplane $y_4 = 0$. We can salvage this issue via multiplication by a factor y_4^{k-1} , where k is the maximal degree of the polynomials that define X^s . Since $k = 3$ for system (2), we define the corresponding Poincaré compactification on \mathbb{S}^3 as

$$\rho(X^s)(y) = y_4^2 X_{\mathbb{S}_\pm}^s(y), \quad (6)$$

that is, $\rho(X^s)$ is defined on \mathbb{S}_\pm^3 as well as the equator. We can think of (6) as a vector field on \mathbb{R}^4 , for which \mathbb{S}^3 is an invariant manifold. Note that, if k were even, the dynamics of $\rho(X^s)(y)$ on the hemisphere \mathbb{S}_-^3 would only be conjugate to X^s by reversing time.

A.2 Projection back to \mathbb{R}^3

As illustrated for the one-dimensional vector field in fig. 13(b), we now project $\mathbb{S}^3 \setminus \{0, 0, 0, -1\} \subset \mathbb{R}^4$ back to \mathbb{R}^3 . We define $g : \mathbb{S}^3 \setminus \{0, 0, 0, -1\} \rightarrow \mathbb{R}^3$ as

$$g(y_1, y_2, y_3, y_4) = \frac{2}{y_4 + 1} (y_1, y_2, y_3),$$

which corresponds to the stereographic projection from the south pole $(0, 0, 0, -1)$ to the hyperplane tangent to \mathbb{S}^3 at the north pole $(0, 0, 0, 1)$. The set $g(\mathbb{S}^3_+)$ is contained in the three-dimensional sphere $\mathbb{S}^2(2) \subset \mathbb{R}^3$ with radius two. Its Jacobian is given by

$$Dg(y) = \frac{2}{y_4 + 1} \begin{pmatrix} 1 & 0 & 0 & \frac{-y_1}{y_4 + 1} \\ 0 & 1 & 0 & \frac{-y_2}{y_4 + 1} \\ 0 & 0 & 1 & \frac{-y_3}{y_4 + 1} \end{pmatrix},$$

and the composition with Df_{\pm} becomes

$$Dg \circ Df_{\pm}(y) = 2 \frac{y_4}{(y_4 + 1)^2} \begin{pmatrix} -y_1^2 + y_4 + 1 & -y_1 y_2 & -y_1 y_3 \\ -y_1 y_2 & -y_2^2 + y_4 + 1 & -y_2 y_3 \\ -y_1 y_3 & -y_2 y_3 & -y_3^2 + y_4 + 1 \end{pmatrix}. \quad (7)$$

Let $\bar{p} = (\bar{x}, \bar{y}, \bar{z}) \in \mathbb{R}^3$ be a point in the new compactified phase space. The inverse of g transforms \bar{p} to the point

$$(y_1, y_2, y_3, y_4) = \frac{4}{\|\bar{p}\|^2 + 4} \left(\bar{x}, \bar{y}, \bar{z}, \frac{4 - \|\bar{p}\|^2}{4} \right) \in \mathbb{S}^3 \setminus \{0, 0, 0, -1\},$$

i.e., $\|g^{-1}(\bar{p})\| = 1$. In these coordinates, (7) becomes

$$Dg \circ Df(\bar{p}) = \frac{4 - \|\bar{p}\|^2}{\|\bar{p}\|^2 + 4} \begin{pmatrix} \frac{-\bar{x}^2 + \bar{y}^2 + \bar{z}^2 + 4}{4} & -\frac{\bar{x}\bar{y}}{2} & -\frac{\bar{x}\bar{z}}{2} \\ -\frac{\bar{x}\bar{y}}{2} & \frac{\bar{x}^2 - \bar{y}^2 + \bar{z}^2 + 4}{4} & -\frac{\bar{y}\bar{z}}{2} \\ -\frac{\bar{x}\bar{z}}{2} & -\frac{\bar{y}\bar{z}}{2} & \frac{\bar{x}^2 + \bar{y}^2 - \bar{z}^2 + 4}{4} \end{pmatrix}.$$

Then the vector field $\overline{X^s} = Dg \circ \rho(X^s) \circ g^{-1} = y_4^2 Dg \circ Df_{\pm} \circ X^s \circ f_{\pm}^{-1} \circ g^{-1}$, defined on \mathbb{R}^3 , can be expressed as

$$\overline{X^s}(\bar{p}) = \left(\frac{4 - \|\bar{p}\|^2}{\|\bar{p}\|^2 + 4} \right)^2 Dg \circ Df \circ X^s \left(\frac{4\bar{x}}{4 - \|\bar{p}\|^2}, \frac{4\bar{y}}{4 - \|\bar{p}\|^2}, \frac{4\bar{z}}{4 - \|\bar{p}\|^2} \right). \quad (8)$$

Note that the solid sphere of radius two is invariant under system (8) and its interior is conjugate to the original system (2) on \mathbb{R}^3 .

In particular, system (8) can be used to track the different equilibria of system (2) in AUTO as they move through infinity, to compute the bifurcation diagrams in fig. 4.

A.3 Analytical study of infinity

In its general form, system (8) is too complex to study the dynamics at infinity, that is, on the boundary $\mathbb{S}^2(2)$ of the compactified phase space. Instead, we study the dynamics at infinity for the differentiable vector field $\rho(X^s)$ as given by (5). To this end, we analyze the dynamics on specific coordinate charts of \mathbb{S}^3 and its equator $\mathbb{S}^2_{\mathbb{R}^4}$ [26, 27]. We consider three different local charts, namely, (U_i, ϕ_i) for $i = 1, 2, 3$, where

$U_i = \{y \in \mathbb{S}^3 : y_i > 0\}$ and $\phi_i : U_i \rightarrow \mathbb{R}^3$; the transformations ϕ_i correspond to the central projections with respect to the tangent planes at the points $(1, 0, 0, 0)$, $(0, 1, 0, 0)$ and $(0, 0, 1, 0)$, respectively, which are similar to the projections f_{\pm}^{-1} used in appendix A.1. The three-dimensional vector fields in these projections contain subsets of the equator $\mathbb{S}_{\mathbb{R}^4}^2$ that correspond to invariant planes. Hence, the problem of studying the dynamics at infinity can be simplified to a study of two-dimensional vector fields [25, 26, 27, 44]. For ease of notation, we use the variables $\tilde{x}, \tilde{y}, \tilde{z}$ and \tilde{w} interchangeably in the different charts. Specifically, \tilde{w} represents the proximity to infinity, that is, $\tilde{w} = 0$ corresponds to the projection of the dynamics infinity in the corresponding chart.

We show the construction for U_1 , that is, the half of \mathbb{S}^3 with $y_1 > 0$. Similar to f_{\pm} , the inverse central projection with the hyperplane tangent to \mathbb{S}^3 at $(1, 0, 0, 0)$ adds 1 as the first component and normalizes the vector. Hence, its inverse $\phi_1(y)$ for $y \in U_1$ is defined as $\phi_1(y) = (y_2/y_1, y_3/y_1, y_4/y_1) =: (\tilde{y}, \tilde{z}, \tilde{w}) \in \mathbb{R}^3$, and the corresponding Jacobian is given by

$$D\phi_1(y) = \frac{1}{y_1} \begin{pmatrix} -\frac{y_2}{y_1} & 1 & 0 & 0 \\ -\frac{y_3}{y_1} & 0 & 1 & 0 \\ -\frac{y_4}{y_1} & 0 & 0 & 1 \end{pmatrix}.$$

then the composition with Df_{\pm} becomes

$$D\phi_1 \circ Df(y) = \frac{1}{y_1} \begin{pmatrix} -\frac{y_2}{y_1} & 1 & 0 \\ -\frac{y_3}{y_1} & 0 & 1 \\ -\frac{y_4}{y_1} & 0 & 0 \end{pmatrix}. \quad (9)$$

Rewriting (9) with respect $(\tilde{y}, \tilde{z}, \tilde{w})$, we have

$$D\phi_1 \circ Df(\tilde{y}, \tilde{z}, \tilde{w}) = \tilde{w} \begin{pmatrix} -\tilde{y} & 1 & 0 \\ -\tilde{z} & 0 & 1 \\ -\tilde{w} & 0 & 0 \end{pmatrix}. \quad (10)$$

Finally, we use the fact that $y_4 = \tilde{w}/(1 + \tilde{y}^2 + \tilde{z}^2 + \tilde{w}^2)^{1/2}$ and (10) to represent the vector field on U_1 , that is, $X_{U_1}^s = D\phi_1 \circ \rho(X^s) \circ \phi_1^{-1}$, as

$$X_{U_1}^s(\tilde{y}, \tilde{z}, \tilde{w}) = \frac{\tilde{w}^2}{1 + \tilde{y}^2 + \tilde{z}^2 + \tilde{w}^2} D\phi_1 \circ Df \circ X^s = \frac{\tilde{w}^3}{1 + \tilde{y}^2 + \tilde{z}^2 + \tilde{w}^2} \begin{pmatrix} -\tilde{y}P^1 + P^2 \\ -\tilde{z}P^1 + P^3 \\ -\tilde{w}P^1 \end{pmatrix}, \quad (11)$$

where $P^j = P^j(1/\tilde{w}, \tilde{y}/\tilde{w}, \tilde{z}/\tilde{w})$ for $j = 1, 2, 3$. The dynamics on the chart U_2 with $\phi_2(y) = (y_1/y_2, y_3/y_2, y_4/y_2) =: (\tilde{x}, \tilde{z}, \tilde{w}) \in \mathbb{R}^3$, where $y \in U_2$, are given by

$$X_{U_2}^s(\tilde{x}, \tilde{z}, \tilde{w}) = \frac{\tilde{w}^2}{1 + \tilde{x}^2 + \tilde{z}^2 + \tilde{w}^2} D\phi_2 \circ Df \circ X^s = \frac{\tilde{w}^3}{1 + \tilde{x}^2 + \tilde{z}^2 + \tilde{w}^2} \begin{pmatrix} -\tilde{x}P^2 + P^1 \\ -\tilde{z}P^2 + P^3 \\ -\tilde{w}P^2 \end{pmatrix}, \quad (12)$$

where $P^j = P^j(\tilde{x}/\tilde{w}, 1/\tilde{w}, \tilde{z}/\tilde{w})$ for $j = 1, 2, 3$. Finally, the dynamics on the chart U_3 with $\phi_3(y) = (y_1/y_2, y_3/y_2, y_4/y_2) =: (\tilde{x}, \tilde{z}, \tilde{w}) \in \mathbb{R}^3$, and $y \in U_3$, are given by

$$X_{U_3}^s(\tilde{x}, \tilde{y}, \tilde{w}) = \frac{\tilde{w}^2}{1 + \tilde{x}^2 + \tilde{y}^2 + \tilde{w}^2} D\phi_3 \circ Df \circ X^s = \frac{\tilde{w}^3}{1 + \tilde{x}^2 + \tilde{y}^2 + \tilde{w}^2} \begin{pmatrix} -\tilde{x}P^3 + P^1 \\ -\tilde{y}P^3 + P^2 \\ -\tilde{w}P^3 \end{pmatrix}, \quad (13)$$

where $P^j = P^j(\tilde{x}/\tilde{w}, \tilde{y}/\tilde{w}, 1/\tilde{w})$ for $j = 1, 2, 3$.

Note that the denominator term in each of the factors for (11), (12) and (13) is strictly positive. Hence, this term can be viewed as a time rescaling that does not alter the dynamics of the vector fields; therefore, it can be omitted. As mentioned before, $\tilde{w} = 0$ is an invariant plane for (11), (12) and (13) that represents infinity. After substitution of the corresponding polynomials and simplification of the expressions, we set $\tilde{w} = 0$ in (11), (12) and (13), which leads to the following three vector fields that represent the dynamics of system (2) at infinity in the corresponding charts:

$$X_{U_1}^s(\tilde{y}, \tilde{z}) : \begin{cases} \dot{\tilde{y}} = -3\alpha\tilde{y}\tilde{z}, \\ \dot{\tilde{z}} = -\alpha(3\tilde{z}^2 + \beta). \end{cases} \quad (14)$$

$$X_{U_2}^s(\tilde{x}, \tilde{z}) : \begin{cases} \dot{\tilde{x}} = 3\alpha\tilde{x}^2\tilde{z}, \\ \dot{\tilde{z}} = -\alpha\beta\tilde{x}^3. \end{cases} \quad (15)$$

$$X_{U_3}^s(\tilde{x}, \tilde{y}) : \begin{cases} \dot{\tilde{x}} = \alpha\tilde{x}^2(\beta\tilde{x}^2 + 3), \\ \dot{\tilde{y}} = \alpha\beta\tilde{x}^3\tilde{y}. \end{cases} \quad (16)$$

Systems (14), (15) and (16) highlight that the dynamics at infinity only depends on the parameters α and β , which are the coefficients of higher powers of the polynomials in system (2). We observe that the three systems each have an integral of motion, namely,

$$H_{U_1}(\tilde{y}, \tilde{z}) = \ln \left(\frac{\tilde{y}^2}{|3\tilde{z}^2 + \beta|} \right), \quad (17)$$

$$H_{U_2}(\tilde{x}, \tilde{z}) = \beta\tilde{x}^2 + 3\tilde{z}^2 \quad \text{and} \quad (18)$$

$$H_{U_3}(\tilde{x}, \tilde{y}) = \ln \left(\frac{|\beta\tilde{x}^2 + 3|}{\tilde{y}^2} \right). \quad (19)$$

Given the parameter chosen in section 2.2, we are interested in how the dynamics at infinity changes as β is varied and $\alpha > 0$.

Note that, for a complete characterization of $\mathbb{S}_{\mathbb{R}^4}^2$, one would also have to study the charts (V_i, σ_i) with $i = 1, 2, 3$, where $V_i = \{y \in \mathbb{S}^3 : y_i < 0\}$ and $\sigma_i : V_i \rightarrow \mathbb{R}^3$ are the central projections to the tangent planes $(-1, 0, 0, 0)$, $(0, -1, 0, 0)$ and $(0, 0, -1, 0)$. We do not study these charts, because the inverse central projections f_{\pm} map to antipodal points and the maximum degree of our polynomials is odd; therefore, the charts U_i and V_i are conjugate to each other via the transformation $p \in U_i \rightarrow -p \in V_i$, for $i = 1, 2, 3$.

A.3.1 Dynamics at infinity when $\beta < 0$

fig. 14 illustrates the dynamics of system (2) at infinity when $\beta < 0$. The first row shows phase portraits of systems (14), (15) and (16) on the charts correspondingly labeled panels (U_1) , (U_2) and (U_3) , respectively. Panel (a) shows how these phase portraits are glued together on a cube and panel (b) representative computed trajectories of system (8) on $\mathbb{S}^2(2)$ for $(a, b, c, \alpha, \beta, \gamma, \mu, \tilde{\mu}) = (0.22, 1, -2, 0.65, -1, 2, 0, 0)$.

In the local chart U_1 , there are two equilibria, at $(\tilde{y}, \tilde{z}) = (0, \pm\sqrt{-\beta/3})$, and their Jacobian matrix is diagonal with eigenvalues $\mp 3\alpha\sqrt{-\beta/3}$ and $\mp 6\alpha\sqrt{-\beta/3}$, respectively; the eigenvectors are $(1, 0)$ for the first and $(0, 1)$ for the second eigenvalue, which is the strong direction. Note that $\tilde{y} = 0$ is invariant, so that the strong (un)stable manifolds are straight lines that coincide. Since the lines $\tilde{z} = \pm\sqrt{-\beta/3}$ are also invariant, both equilibria have linear weak (un)stable manifolds as well; we denote these straight lines by l_{\pm} . The curves l_{\pm} connect the points $(0, 2, 0)$ and $(0, -2, 0)$ in the phase space of (8).

In the local chart U_2 , as we see from equation (18), solutions of system (15) are tangent to the family of hyperbolas with asymptotes $\tilde{z} = \pm\tilde{x}\sqrt{-\beta/3}$ when $\beta < 0$. The curves l_{\pm} correspond to these asymptotes in the local chart U_2 . They are the only trajectories that converge to the origin, which is the point $(0, 2, 0)$ of $\mathbb{S}^2(2)$. The \tilde{z} -axis is a family of non-hyperbolic equilibria of system (15) with one stable direction when $\tilde{x} < 0$ and one unstable direction when $\tilde{x} > 0$.

The phase portrait of system (16) in the chart U_3 with $\beta < 0$ is similar to that of system (14) after the transformation $(\tilde{y}, \tilde{z}) \mapsto (-\tilde{y}, \tilde{x})$ and rotation by $-\frac{\pi}{2}$; panel (U_3) of fig. 14 shows that the \tilde{x} -axis is invariant and corresponds to the strong manifolds of the two equilibria $(\pm\sqrt{-3/\beta}, 0)$; also, the vertical lines

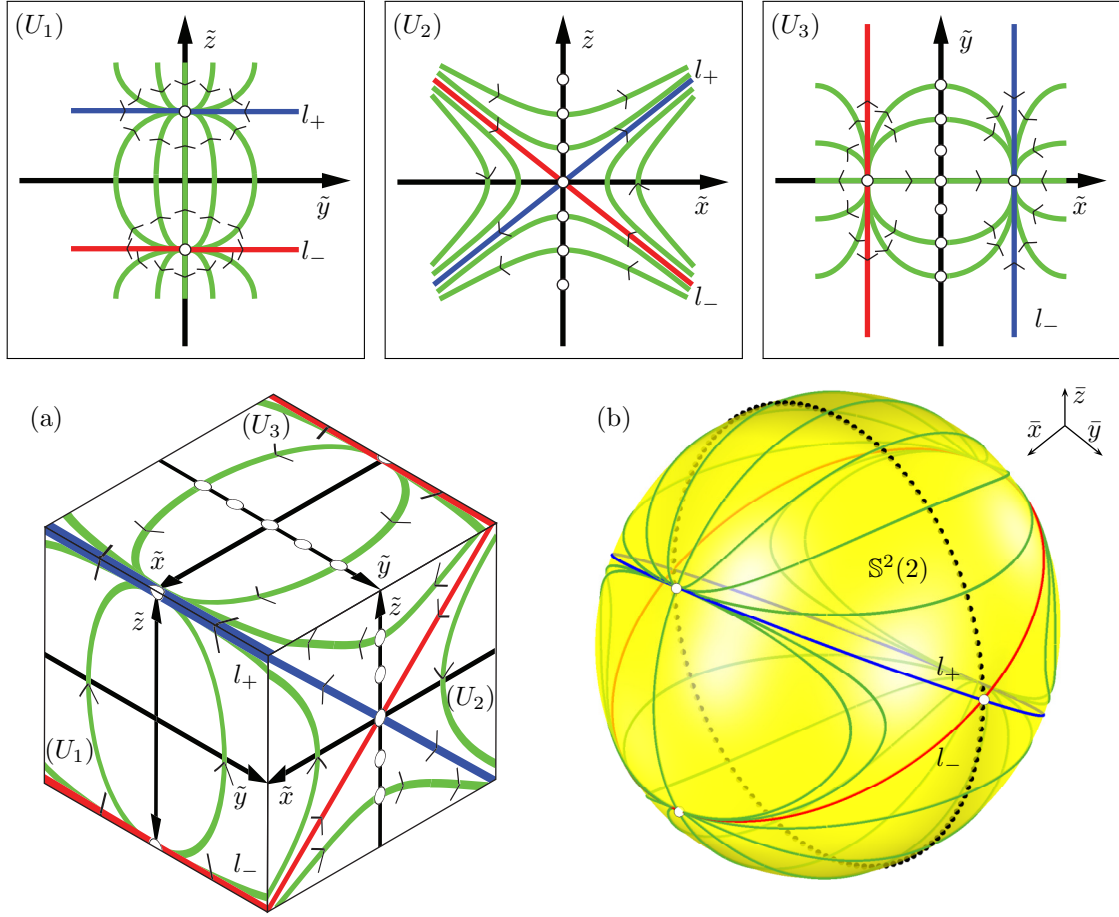


Figure 14: Dynamics of system (2) at infinity when $\beta < 0$; the first row shows different coordinate charts that fit together as neighboring faces on a cube in panel (a). The sphere in panel (b) shows computed trajectories (green) on $S^2(2)$ for the compactified system (8) for $(a, b, c, \alpha, \beta, \gamma, \mu, \tilde{\mu}) = (0.22, 1, -2, 0.65, -1, 2, 0, 0)$.

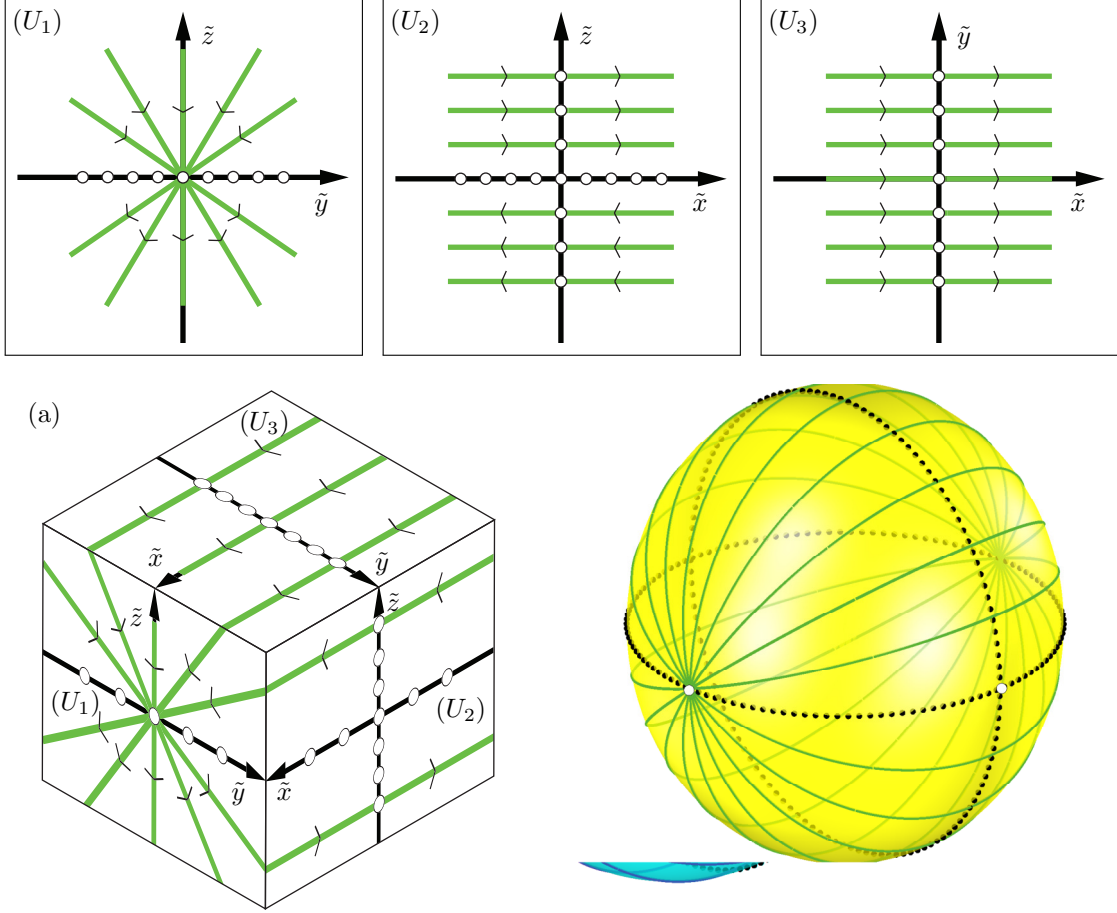


Figure 15: Dynamics of system (2) at infinity when $\beta = 0$; the first row shows different coordinate charts that fit together as neighboring faces on a cube in panel (a). The sphere in panel (b) shows computed trajectories (green) on $S^2(2)$ for the compactified system (8) for $(a, b, c, \alpha, \beta, \gamma, \mu, \tilde{\mu}) = (0.22, 1, -2, 0.65, 0, 2, 0, 0)$.

$\tilde{x} = \pm\sqrt{-3/\beta}$ are invariant and correspond to the projections of l_{\pm} under ϕ_3 . However, due to the factor \tilde{x}^2 in the equations, the \tilde{z} -axis is a set of non-hyperbolic equilibria just as for system (15).

The cube and sphere in the second row of fig. 14 show how the curves l_{\pm} connect the two nodes in the chart U_1 with the equilibrium $(0, 0)$ in the chart U_3 .

A.3.2 Dynamics at infinity when $\beta = 0$

Systems (14)-(16) for $\beta = 0$ become

$$X_{U_1^\infty}^s(\tilde{y}, \tilde{z}) : \begin{cases} \dot{\tilde{y}} = -3\alpha\tilde{y}\tilde{z}, \\ \dot{\tilde{z}} = -3\alpha\tilde{z}^2, \end{cases} \quad X_{U_2^\infty}^s(\tilde{x}, \tilde{z}) : \begin{cases} \dot{\tilde{x}} = 3\alpha\tilde{x}^2\tilde{z}, \\ \dot{\tilde{z}} = 0, \end{cases} \quad X_{U_3^\infty}^s(\tilde{x}, \tilde{y}) : \begin{cases} \dot{\tilde{x}} = 3\alpha\tilde{x}^2, \\ \dot{\tilde{y}} = 0. \end{cases}$$

The corresponding phase portraits are shown in the first row of fig. 15; in the different charts U_1 , U_2 and U_3 . Panel (U_1) of fig. 15 shows a sketch of the phase portrait (14) for $\beta = 0$. Note that the \tilde{y} -axis consists of non-hyperbolic equilibria and the \tilde{z} -axis is invariant. In fact, its first integral of motion (17) can be simplified to

$$H_{U_1}(\tilde{y}, \tilde{z}) = \frac{\tilde{y}}{\tilde{z}},$$

which means that any straight line through the origin is invariant. We can think of the origin as a saddle-node equilibrium; indeed, as $\beta < 0$ increases towards 0, the two equilibria from fig. 14 move closer together and

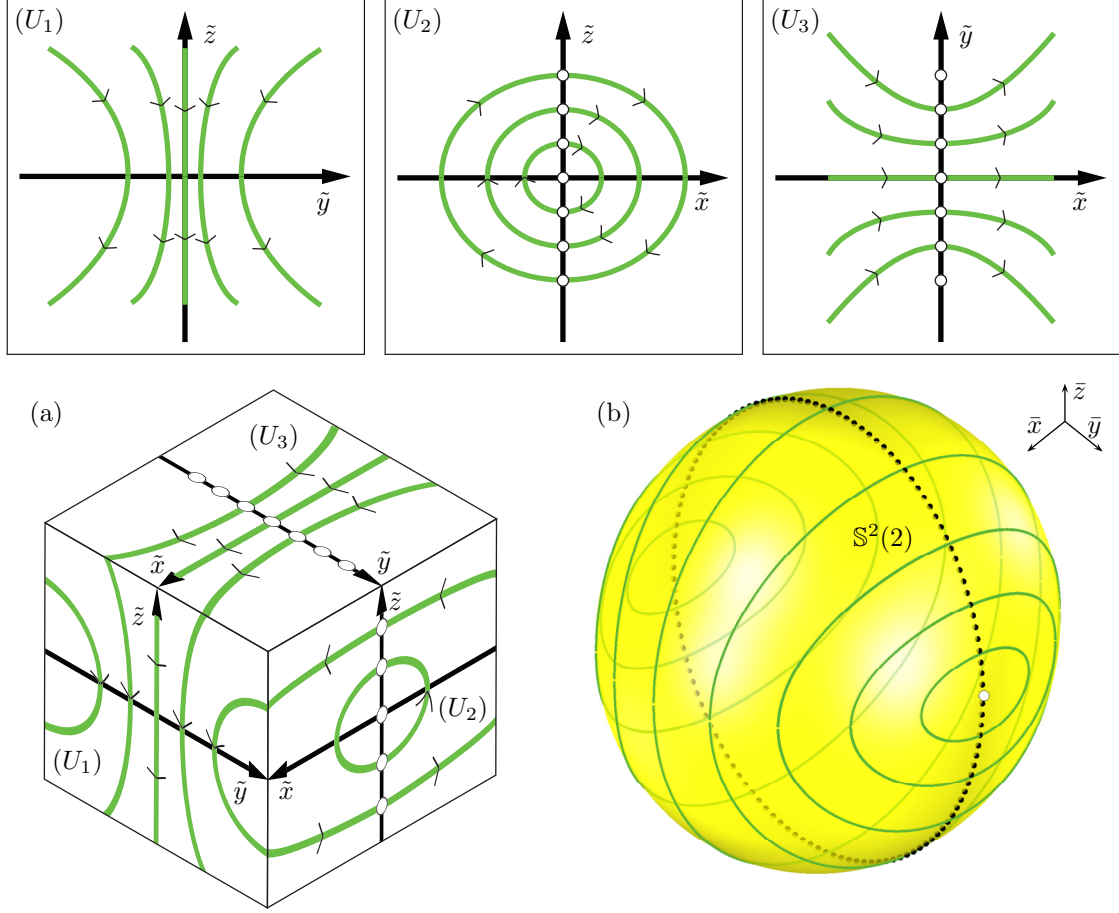


Figure 16: Dynamics of system (2) at infinity when $\beta > 0$; the first row shows different coordinate charts that fit together as neighboring faces on a cube in panel (a). The sphere in panel (b) shows computed trajectories (green) on $\mathbb{S}^2(2)$ for the compactified system (8) for $(a, b, c, \alpha, \beta, \gamma, \mu, \tilde{\mu}) = (0.22, 1, -2, 0.65, 1, 2, 0, 0)$.

eventually, at $\beta = 0$, merge at the origin. Similarly, the lines l_{\pm} meet at the \tilde{y} -axis for $\beta = 0$ and become a family of non-hyperbolic equilibria.

Panel (U_2) of fig. 15 shows a sketch of the phase portrait (15) for $\beta = 0$ and illustrates that the dynamics in the local chart U_2 are reduced to one-dimensional dynamics. The \tilde{x} - and \tilde{z} -axes are families of degenerate equilibria, and the horizontal lines are invariant. The non-hyperbolic equilibria on the \tilde{z} -axis are degenerate saddle-node points.

The dynamics in system (16) on U_3 are also reduced to one-dimensional dynamics. The \tilde{y} -axis is a set of degenerate saddle-node equilibria and the horizontal lines are invariant. In contrast to the limit argument used for the chart U_1 , the two hyperbolic equilibria that exist for $\beta < 0$ do not disappear in a saddle-node bifurcation at $\beta = 0$; instead they go to infinity in U_3 . More precisely, these equilibria disappear at a saddle-node bifurcation on the local chart U_1 and its antipodal chart V_1 , which both cannot be seen in the local chart U_3 .

fig. 15(a) shows how the different charts can be glued together to form a cube. As shown in fig. 15(b), we also computed trajectories of system (8) on its invariant sphere $\mathbb{S}^2(2)$; here, $(a, b, c, \alpha, \beta, \gamma, \mu, \tilde{\mu}) = (0.22, 1, -2, 0.65, 0, 2, 0, 0)$. Note that the horizontal trajectories in the charts U_2 and U_3 are translated to curves on $\mathbb{S}^2(2)$ that connect the poles at $(2, 0, 0)$ and $(-2, 0, 0)$. The great circles $\tilde{x} = 0$ and $\tilde{z} = 0$ both consist of degenerate equilibria.

A.3.3 Dynamics at infinity when $\beta > 0$

fig. 16 shows the corresponding phase portraits of system (2) with $\beta > 0$ on the charts at infinity in the correspondingly labeled panels (U_1), (U_2) and (U_3), respectively. On U_1 there are no equilibria when $\beta > 0$ and the \tilde{z} -axis is invariant under the flow. The first integral of motion (17) defines the family of radical functions $\tilde{y} = \pm\sqrt{e^c(3\tilde{z}^2 + \beta)}$, for $c \in \mathbb{R}$. While, on the chart U_2 , the first integral of motion (18) for system (15) defines a family of ellipses that are oriented clockwise and the \tilde{z} -axis is a family of non-hyperbolic equilibria. Finally, on the chart U_3 , system (16) has a family of non-hyperbolic equilibria on the \tilde{y} -axis. As in the local chart U_1 , its first integral of motion (19) defines the family of radical functions $\tilde{y} = \pm\sqrt{e^c(\beta\tilde{x}^2 + 3)}$, for $c \in \mathbb{R}$; where the \tilde{x} -coordinate increases with time.

Panel (a) of fig. 16 shows how these projections fit together on a cube for $\beta > 0$. Panel(b) shows computed trajectories of system (8) on $\mathbb{S}^2(2)$. In particular, note how each trajectory in U_1 is translated to a curve that connects equilibria $(0, \bar{y}, \bar{z})$ and $(0, \bar{y}, -\bar{z})$. The local charts U_2 and U_3 imply that the \bar{z} -coordinate of the trajectories with $\bar{x} > 0$ decreases with time, while it increases for trajectories with $\bar{x} < 0$; this agrees with the orientation computed for the trajectories on $\mathbb{S}^2(2)$.

B Boundary value problem formulations

More often than not, it is impossible to compute Floquet multipliers of a given saddle periodic orbit explicitly, let alone approximate the corresponding eigenbundles and global stable and unstable manifolds. We employ continuation of a suitable two-point boundary value problems (2PBVP) with the software package AUTO [5, 7] to solve these problems for a three-dimensional system of the form (1). The idea behind 2PBVP continuation is to represent the object of interest as a one-parameter family of finite-time orbit segments of system (1) that satisfy suitable boundary conditions; see [6], for general background of this approach.

As discussed in [1, 21] any trajectory of (1) over the finite-time interval $[0, T]$ can be represented as an orbit segment $u : [0, 1] \rightarrow \mathbb{R}^n$ over the interval $[0, 1]$ that satisfies equation

$$\dot{u} = Tf(u, \mu), \quad (20)$$

which is a time-rescaled version of system (1) with (original) integration time $T > 0$. During the continuation, we impose additional boundary conditions at $u(0)$ and $u(1)$.

We refer to [9] for an in-depth discussion of the 2PBVP formulation needed to calculate the Floquet multipliers of a saddle periodic orbit and their respective tangent bundles. The 2PBVP formulation and computation of two-dimensional stable and unstable manifolds of saddle periodic orbits (as well as equilibria) and their intersection sets with a sphere can be found in [2, 21].

In the following sections, we present the 2PBVP formulation for the following:

1. The intersection set of the stable manifold of a saddle periodic orbit with a tubular neighborhood; this is used for the computation of the local stable and unstable manifolds of the saddle periodic orbits in fig. 2.
2. The computation and continuation of a periodic orbit at the moment when two Floquet multipliers change from being real to complex conjugate; this allows us to find the curves \mathbf{CC}^+ and \mathbf{CC}^- in fig. 5 and fig. 11.

B.1 The intersection set of the manifold of a saddle periodic orbit with a tubular section

The orientation of a two-dimensional stable manifold of a saddle periodic orbit can be illustrated by computing a first local portion. The approach described here finds this portion as the manifold computed up to its first intersection with a tubular section of small radius $d \geq 0$ around the periodic orbit; see rows 1 and 2 of fig. 2. Our formulation also works particularly well if the Floquet multiplier associated with the manifold is close to 0 in magnitude.

Let Γ be a saddle periodic orbit in \mathbb{R}^3 and assume that we wish to compute a first portion of its two-dimensional stable manifold $W^s(\Gamma)$. We extend the system from three equations to six, so that we effectively

consider two different orbit segments of (1):

$$\begin{cases} \dot{v}_\Gamma = T_\Gamma f(v_\Gamma(t), \mu), & v_\Gamma \in \Gamma, \\ \dot{u} = Tf(u(t), \mu), & u \in \mathbb{R}^3. \end{cases} \quad (21)$$

The segment $v_\Gamma(t)$ is meant to represent Γ . Hence, T_Γ is the period and we impose the boundary condition:

$$v_\Gamma(1) - v_\Gamma(0) = 0. \quad (22)$$

The idea is that $u(t)$ represents a solution trajectory with integration time T that is contained in $W^s(\Gamma)$. Since $u(t)$ converges to Γ as t goes to infinity, we stipulate that $u(1)$ lies close to Γ , in an approximate one-dimensional fundamental domain \mathcal{F}_δ of the linear approximation of $W^s(\Gamma)$. Every (approximated) trajectory in $W^s(\Gamma)$ intersects \mathcal{F}_δ exactly once, and this domain is parametrized by the variation of δ in a closed interval; see [2] for details. The parameterized boundary condition:

$$u(1) \in \mathcal{F}_\delta \quad (23)$$

introduces a free parameter δ on top of the (free) parameters T_Γ and T .

The tubular section with radius d around Γ is defined as

$$T_\Gamma^d := \left\{ x \in \mathbb{R}^3 : \min_{y \in \Gamma} \|x - y\|_{\mathbb{R}^3} = d \right\},$$

where $\|\cdot\|_{\mathbb{R}^3}$ is the Euclidean norm in \mathbb{R}^3 . We are interested in orbit segments u of (21) that satisfy (22) and (23), and also $u(0) \in T_\Gamma^d$. The family of all such orbit segments forms the first portion of $W^s(\Gamma)$ and its end points $u(\cdot)$ form the intersection set $W^s(\Gamma) \cap T_\Gamma^d$, which is a one-dimensional curve. We parametrize this set on T_Γ^d via the points on Γ that achieve the minimum d for the point $u(0)$, that is, we use the orbit segment v_Γ of system (21) to track $W^s(\Gamma) \cap T_\Gamma^d$. We impose the following two boundary conditions:

$$\langle f(v_\Gamma(0), \mu), u(0) - v_\Gamma(0) \rangle = \alpha, \quad (24)$$

$$\|v_\Gamma(0) - u(0)\|_{\mathbb{R}^3} = d, \quad (25)$$

where $\langle \cdot, \cdot \rangle$ is the dot product. When $\alpha = 0$, condition (24) implies that $u(0)$ lies in the plane normal to Γ at $v_\Gamma(0)$; this is a necessary condition for $v_\Gamma(0)$ to achieve the minimal distance of $u(0)$ to Γ . Condition (25) defines the radius of the tubular section, that is, it ensures that $u(0)$ lies on T_Γ^d . The sequence of steps to follow in AUTO is:

1. Pre-compute from another run a periodic solution $v_\Gamma(t)$ with period T_Γ and its respective fundamental domain \mathcal{F}_δ .
2. Extend the system with the 2PBVP-formulation (21) to (25), and define a first solution $u = u(0) = u(1) \in \mathcal{F}_\delta$ with $T = 0$.
3. Continue in α and let d vary until $\alpha = 0$. This step rotates $v_\Gamma(0)$ along Γ until $\|u(0) - v_\Gamma(0)\|_{\mathbb{R}^3}$ is minimal. Here, $T = 0$ and d are fixed, and T_Γ is a continuation parameter.
4. Fix $\alpha = 0$ and continue in d until a suitable distance is reached. Here, both T and T_Γ are free, but T_Γ will remain almost constant and T increases.
5. Fix d and continue in δ while T and T_Γ vary. The δ -family of orbit segments computed in this run forms $W^s(\Gamma)$ with the local part of $u(0) \in T_\Gamma^d$.

If Γ is orientable, $W^s(\Gamma) \cap T_\Gamma^d$ consists of two closed curves; if Γ is non-orientable, on the other hand, $W^s(\Gamma) \cap T_\Gamma^d$ is a single closed curve that is found in one continuation run during which $v_\Gamma(0)$ rotates along Γ twice.

B.2 BVP formulation for the computation of the curves \mathbf{CC}^+ and \mathbf{CC}^-

The strong stable manifold of an attracting periodic orbit Γ^a disappears when its Floquet multipliers change from being real to complex conjugate. The curve \mathbf{CC}^+ and \mathbf{CC}^- represent the moment that two real positive or negative Floquet multipliers become complex conjugate, respectively. We use the 2PBVP formulation presented in [9] to compute the Floquet multipliers and their respective bundles, and follow these steps in AUTO:

1. Continue the periodic orbit Γ^a with one of its Floquet multipliers and associated eigenbundle in a system parameter μ_1 . Here, the period T_Γ^a of Γ^a varies.
2. The moment when the Floquet multiplier becomes complex is detected in AUTO as a fold point. One has to be careful, because AUTO also marks an actual saddle-node bifurcation of periodic orbits as a fold point, which occurs when the Floquet multiplier is 1.
3. Compute the locus of the fold point by continuing in μ_1 and a second system parameter μ_2 . Here, the period T_Γ^a and the value of the Floquet multiplier are free parameters.

The set of points μ_1 and μ_2 computed in step 3 represents the curve \mathbf{CC}^+ or \mathbf{CC}^- .

Acknowledgments

The authors thank Pablo Aguirre for helpful discussion on homoclinic flip bifurcations and the computation of manifolds in AUTO.

References

- [1] P. AGUIRRE, B. KRAUSKOPF, AND H. M. OSINGA, *Global invariant manifolds near homoclinic orbits to a real saddle: (non)orientability and flip bifurcation*, SIAM J. Appl. Dyn. Syst., 12 (2013), pp. 1803–1846.
- [2] R. C. CALLEJA, E. J. DOEDEL, A. R. HUMPHRIES, A. LEMUS-RODRIGUEZ, AND E. B. OLDEMAN, *Boundary-value problem formulations for computing invariant manifolds and connecting orbits in the circular restricted three body problem*, Celest. Mech. Dyn. Astron., 114 (2012), pp. 77–106.
- [3] A. R. CHAMPNEYS, Y. KUZNETSOV, AND B. SANDSTEDE, *A numerical toolbox for homoclinic bifurcation analysis*, Internat. J. Bifur. Chaos Appl. Sci. Engrg, 6 (1996), pp. 867–887.
- [4] B. DENG, *Homoclinic twisting bifurcations and cusp horseshoe maps*, J. Dynam. Differential Equations, 5 (1993), pp. 417–467.
- [5] E. J. DOEDEL, *Auto: A program for the automatic bifurcation analysis of autonomous systems*, Congr. Numer., 30 (1981), pp. 265–284.
- [6] E. J. DOEDEL, *Lectures notes on numerical analysis of nonlinear equations*, in Numerical Continuation Methods for Dynamical Systems: Path following and boundary value problems, B. Krauskopf, H. M. Osinga, and J. Galán-Vioque, eds., Springer Netherlands, 1st ed., 2007, pp. 1–50.
- [7] E. J. DOEDEL AND B. E. OLDEMAN, *AUTO-07p: Continuation and Bifurcation Software for Ordinary Differential Equations*, Department of Computer Science, Concordia University, Canada, 2010. With major contributions from A. R. Champneys, F. Dercole, T. F. Fairgrieve, Y. Kuznetsov, R. C. Paffenroth, B. Sandstede, X. J. Wang and C. H. Zhang; available at <http://www.cmv1.cs.concordia.ca/>.
- [8] F. DUMORTIER, J. LLIBRE, AND J. C. ARTÉS, *Qualitative Theory of Planar Differential Systems*, Springer Berlin Heidelberg, 2006.
- [9] J. P. ENGLAND, B. KRAUSKOPF, AND H. M. OSINGA, *Computing one-dimensional global manifolds of Poincaré maps by continuation*, SIAM J. Appl. Dyn. Syst., 4 (2005), pp. 1008–1041.

- [10] G. B. ERMENTROUT AND D. H. TERMAN, *Mathematical Foundations of Neuroscience*, Springer-Verlag New York, 2010.
- [11] A. GOLMAKANI AND A. J. HOMBURG, *Lorenz attractors in unfoldings of homoclinic-flip bifurcations*, *Dynam. Systems*, 26 (2011), pp. 61–76.
- [12] E. GONZÁLEZ VELASCO, *Generic properties of polynomial vector fields at infinity*, *Trans. Amer. Math. Soc.*, 143 (1969), pp. 201–222.
- [13] J. GUCKENHEIMER AND P. HOLMES, *Nonlinear Oscillations, Dynamical Systems, and Bifurcations of Vector Fields*, Springer-Verlag New York, 1st ed., 1983.
- [14] A. L. HODGKIN AND A. F. HUXLEY, *A quantitative description of membrane current and its application to conduction and excitation in nerve*, *J. Physiol.*, 117 (1952), pp. 500–544.
- [15] A. J. HOMBURG, H. KOKUBU, AND M. KRUPA, *The cusp horseshoe and its bifurcations in the unfolding of an inclination-flip homoclinic orbit*, *Ergodic Theory Dynam. Systems*, 14 (1994), pp. 667–693.
- [16] A. J. HOMBURG, H. KOKUBU, AND V. NAUDOT, *Homoclinic-doubling cascades*, *Arch. Rational Mech. Analysis*, (2001), pp. 195–243.
- [17] A. J. HOMBURG AND B. KRAUSKOPF, *Resonant homoclinic flip bifurcations*, *J. Dynam. Differential Equations*, 12 (2000), pp. 807–850.
- [18] A. J. HOMBURG AND B. SANDSTEDT, *Homoclinic and heteroclinic bifurcations in vector fields*, in *Handbook of Dynamical Systems*, H. W. Broer, B. Hasselblatt, and F. Takens, eds., vol. 3rd, Elsevier, 2010, pp. 381–509.
- [19] J. P. KEENER AND J. SNEYD, *Mathematical Physiology*, Springer-Verlag New York, 2nd ed., 2009.
- [20] M. KISAKA, H. KOKUBU, AND H. OKA, *Bifurcations to n -homoclinic orbits and n -periodic orbits in vector fields*, *J. Dynam. Differential Equations*, 5 (1993), pp. 305–357.
- [21] B. KRAUSKOPF AND H. M. OSINGA, *Computing invariant manifolds via the continuation of orbit segments*, in *Numerical Continuation Methods for Dynamical Systems: Path following and boundary value problems*, B. Krauskopf, H. M. Osinga, and J. Galán-Vioque, eds., Springer Netherlands, 2007, pp. 117–154.
- [22] Y. A. KUZNETSOV, *Elements of Applied Bifurcation Theory*, Springer-Verlag New York, 3rd ed., 2004.
- [23] D. LINARO, A. CHAMPNEYS, M. DESROCHES, AND M. STORACE, *Codimension-two homoclinic bifurcations underlying spike adding in the hindmarsh-rose burster*, *SIAM J. Appl. Dyn. Syst.*, 11 (2012), pp. 939–962.
- [24] X. LIU, L. SHI, AND D. ZHANG, *Homoclinic flip bifurcation with a nonhyperbolic equilibrium*, *Nonlinear Dyn.*, 69 (2012), pp. 655–665.
- [25] J. LLIBRE AND C. VIDAL, *Global dynamics of the kummer–schwarz differential equation*, *Mediterr. J. Math.*, 11 (2014), p. 477–486.
- [26] M. MESSIAS, *Dynamics at infinity and the existence of singularly degenerate heteroclinic cycles in the lorenz system*, *J. Phys. A*, 42 (2009).
- [27] M. MESSIAS, *Dynamics at infinity of a cubic chua’s system*, *Internat. J. Bifur. Chaos Appl. Sci. Engrg.*, 21 (2011), pp. 333–340.
- [28] C. A. MORALES AND M. PACIFICO, *Inclination-flip homoclinic orbits arising from orbit-flip*, *Nonlinearity*, 14 (2001), pp. 379–393.
- [29] V. NAUDOT, *Strange attractor in the unfolding of an inclination-flip homoclinic orbit*, *Ergodic Theory Dynam. Systems*, 16 (1996), pp. 1071–1086.

- [30] V. NAUDOT, *A strange attractor in the unfolding of an orbit-flip homoclinic orbit*, Dyn. Syst., 17 (2002), pp. 45–63.
- [31] B. E. OLDEMAN, B. KRAUSKOPF, AND A. R. CHAMPNEYS, *Numerical unfoldings of codimension-three resonant homoclinic flip bifurcations*, Nonlinearity, 14 (2001), pp. 597–621.
- [32] H. M. OSINGA, *Nonorientable manifolds in three-dimensional vector fields*, Internat. J. Bifur. Chaos Appl. Sci. Engrg., 13 (2003), pp. 553–570.
- [33] J. PALIS AND W. DE MELO, *Geometric Theory of Dynamical Systems*, Springer US, 1982.
- [34] L. PERKO, *Differential Equations and Dynamical Systems*, Springer-Verlag New York, 2nd ed., 1996.
- [35] H. POINCARÉ, *New Methods of Celestial Mechanics*, AIP-Press, 1st ed., 1992. Originally published as *Les Méthodes nouvelles de la Mécanique celeste*. Edited in english by David Goroff.
- [36] R. ROY, T. W. MURPHY, J. T. D. MAIER, Z. GILLS, AND E. R. HUNT, *Dynamical control of a chaotic laser: Experimental stabilization of a globally coupled system*, Phys. Rev. Lett., 68 (1992), pp. 1259–1262.
- [37] D. RUELLE AND F. TAKENS, *On the nature of turbulence*, Commun. Math. Phys., 20 (1971), pp. 167–192.
- [38] B. SANDSTEDE, *Verzweigungstheorie homokliner Verdopplungen*, PhD thesis, University of Stuttgart, 1993.
- [39] B. SANDSTEDE, *Constructing dynamical systems having homoclinic bifurcation points of codimension two*, J. Dynam. Differential Equations, 9 (1997), pp. 269–288.
- [40] L. P. SHILNIKOV, *On the generation of a periodic motion from trajectories doubly asymptotic to an equilibrium state of saddle type*, Mat. Sb. (N.S.), 77(119) (1968), pp. 461–472.
- [41] L. P. SHILNIKOV, A. L. SHILNIKOV, D. V. TURAEV, AND L. O. CHUA, *Methods of Qualitative Theory in Nonlinear Dynamics (Part I)*, vol. 4, World Scientific, Singapore, 1998.
- [42] S. H. STROGATZ, *Nonlinear Dynamics and Chaos: With Applications to Physics, Biology, Chemistry and Engineering*, Addison-Wesley, Reading, MA, 1994.
- [43] H. L. SWINNEY AND J. P. GOLLUB, *Hydrodynamic Instabilities and the Transition to Turbulence*, Springer Berlin Heidelberg, 1985.
- [44] R. M. TUDORAN AND A. GIRBAN, *On a hamiltonian version of a three-dimensional lotka–volterra system*, Nonlinear Anal. Real World Appl., 13 (2012), pp. 2304–2312.
- [45] S. M. WIECZOREK, *Global bifurcation analysis in laser systems*, in Numerical Continuation Methods for Dynamical Systems: Path following and boundary value problems, B. Krauskopf, H. M. Osinga, and J. Galán-Vioque, eds., Springer Netherlands, 2007, pp. 177–220.
- [46] S. WIGGINS, *Introduction to Applied Nonlinear Dynamical Systems and Chaos*, Springer-Verlag New York, 2nd ed., 2003.
- [47] T. XING, R. BARRIO, AND A. SHILNIKOV, *Symbolic quest into homoclinic chaos*, Internat. J. Bifur. Chaos Appl. Sci. Engrg., 24 (2014).